Quaternary Science Reviews
June 2022, Volume 286 Pages 107548 (21p.)
https://doi.org/10.1016/j.quascirev.2022.107548
https://archimer.ifremer.fr/doc/00770/88231/

Cosmogenic 10Be constraints on deglacial snowline rise in the Southern Alps, New Zealand

Tielidze Levan G. [1, 2, 3, *], Eaves Shaun R. [1, 2], Norton Kevin P. [2], Mackintosh Andrew N. [4], Hidy Alan J. [5]

[1] Antarctic Research Centre, Victoria University of Wellington, P.O. Box 600, 6140, Wellington, New Zealand
[2] School of Geography, Environment and Earth Sciences, Victoria University of Wellington, P.O. Box 600, 6140, Wellington, New Zealand
[3] chool of Natural Sciences and Medicine, Ilia State University, Cholokashvili Ave 3/5, 0162, Tbilisi, Georgia
[4] School of Earth, Atmosphere and Environment, Monash University, Wellington Road, Clayton, Melbourne, 3168, Australia
[5] Center for Accelerator Mass Spectrometry, Lawrence Livermore National Laboratory, 7000 East Avenue, Livermore, CA, 94550, USA

* Corresponding author : Levan G. Tielidze, email address : tielidzelevan@gmail.com

Abstract :

Geochronological dating of glacial landforms, such as terminal and lateral moraines, is useful for determining the extent and timing of past glaciation and for reconstructing the magnitude and rate of past climate changes. In the Southern Alps of New Zealand, well-dated glacial geomorphological records constrain the last glacial cycle across much of the Waitaki River basin (e.g. Ōhau, Pukaki, Tekapo) but its southern sector such as the Ahuriri River valley remains comparatively unconstrained. Recently, there has been debate on the scale and rapidity of mountain glacier retreat during the last glacial termination, particularly the 20–17 ka period in New Zealand. Missing from this debate is well-constrained equilibrium-line altitude (ELA) and associated temperature reconstructions, particularly over the period around 17 ka, which can help us to develop a more complete picture of how past temperature changes drove glacier retreat. Here we report the first glacial chronology dataset from the Last Glacial Maximum (LGM) and subsequent deglaciation from the Ahuriri River valley, Southern Alps, New Zealand (44°23′54″S, 169°39′48″E) based on 38 beryllium-10 (10Be) surface-exposure ages from terminal moraine systems and glaciated bedrock situated at the lower and middle sections of the valley. Our results show that the former Ahuriri Glacier reached its maximum extent at 19.8 ± 0.3 ka, which coincides with the global Last Glacial Maximum. By 16.7 ± 0.3 ka, the glacier had retreat ~18 km up-valley suggesting at least ~43% glacier-length loss relative to its full LGM extent. This deglaciation was accompanied by the formation of a shallow proglacial lake. Using the accumulation area ratio (AAR) method, we estimate that the ELA was lower than present by ~880 m (~1120 m a.s.l.) at 19.8 ± 0.3 ka, and ~770 m lower (~1230 m a.s.l.) at 16.7 ± 0.3 ka. Applying an estimate for temperature lapse rate, this ELA anomaly implies that local air temperature was 5 ± 1 °C colder than present (1981–2010) at 19.8 ± 0.3 ka, while it was 4.4 ± 0.9 °C colder at 16.7 ± 0.3 ka, assuming no change in precipitation. The substantial glacier retreat in response to a relatively small accompanying increases in ELA (110 m) and temperature (0.6 °C) may have been a result of the high glacier-length sensitivity of this glacier system due to its low gradient of former ice surface. Our low warming estimate differs markedly from other deglaciation studies, specifically from Rakaia River valley, which reports a much larger temperature increase at the onset of the last deglaciation. This precisely-dated moraine record along with reconstructed ELA as proxies for atmospheric conditions, provides new insight into post LGM glacier behaviour and climate conditions in New Zealand.

Keywords : Last glacial maximum, Last deglaciation, Equilibrium line altitude, Past climate, Southern Alps, New Zealand

1 Introduction

Past glacial maxima and their terminations provide important information on the dynamics of the climate system, particularly the relationships between the atmosphere, hydrosphere and the cryosphere (Clark et al., 2009; Denton et al., 2010). Such information is fundamental for assessing the stability of Earth's climate considering ongoing climate change (IPCC, 2019). Identifying the timing of key climate transitions during past warming episodes, such as the last glacial termination, may help to understand the future evolution of Earth's climate system (e.g. Denton et al., 2021).

Mountain glaciers are highly sensitive to climate change (Oerlemans and Fortuin, 1992) and provide proxy information for regional and global climate (Oerlemans, 2005; Mackintosh et al., 2017). Exposure dating of moraines using terrestrial cosmogenic nuclides such as ^{10}Be provides new information on the duration, timing, and scale of the Late Quaternary glaciation (Balco, 2011, 2020). The high sensitivity of glaciers to climate change also permits quantitative reconstruction of past temperature and precipitation (Mackintosh et al., 2017), which may be used to test hypotheses about past climate change mechanisms (e.g. Dowling et al., 2021).

Late Quaternary glacier-based climate reconstructions from the Southern Alps are of particular interest since very few glacierized mountain regions exist in the mid latitudes of the Southern Hemisphere (Figure 1). The climate in New Zealand and the southwest Pacific region was markedly different from present during the last glacial termination (Lorrey and Bostock, 2017). Despite the high utility of glaciers as climatic indicators, glacier-based estimates of the onset and rate of air temperature rise during this time-period lack consensus. Several studies advocate for rapid deglaciation, in response to regional warming beginning at 18 ka (Putnam et al., 2013b; Barrell et al., 2019; Denton et al., 2021). However, this is countered by suggestions that proglacial lake development at such sites may have compromised the relationship between glacier length and surface mass balance (Shulmeister et al., 2010; 2018a) and that air temperatures may have remained depressed until 15-16 ka (Rother et al., 2014).

These uncertainties remain, despite relatively abundant moraine chronologies, in large part due to the paucity of associated quantitative climate reconstructions. While glaciers are of high utility as climate proxies, the magnitude of length changes is not only reflective of regional climate, but also glacier geometry, which is largely reflects catchment topography. Qualitative inference of climate change from chronological information alone, may thus overlook key aspects of glacier response to climate change (e.g. Eaves et al., 2019). In this study we pair cosmogenic ^{10}Be exposure dating of a sequence of glacial landforms that are sufficiently preserved to permit reconstruction of past glacier equilibrium line altitude, thus affording quantitative information of both the timing and magnitude of climatic change in the Southern Alps at the onset of the glacial termination.

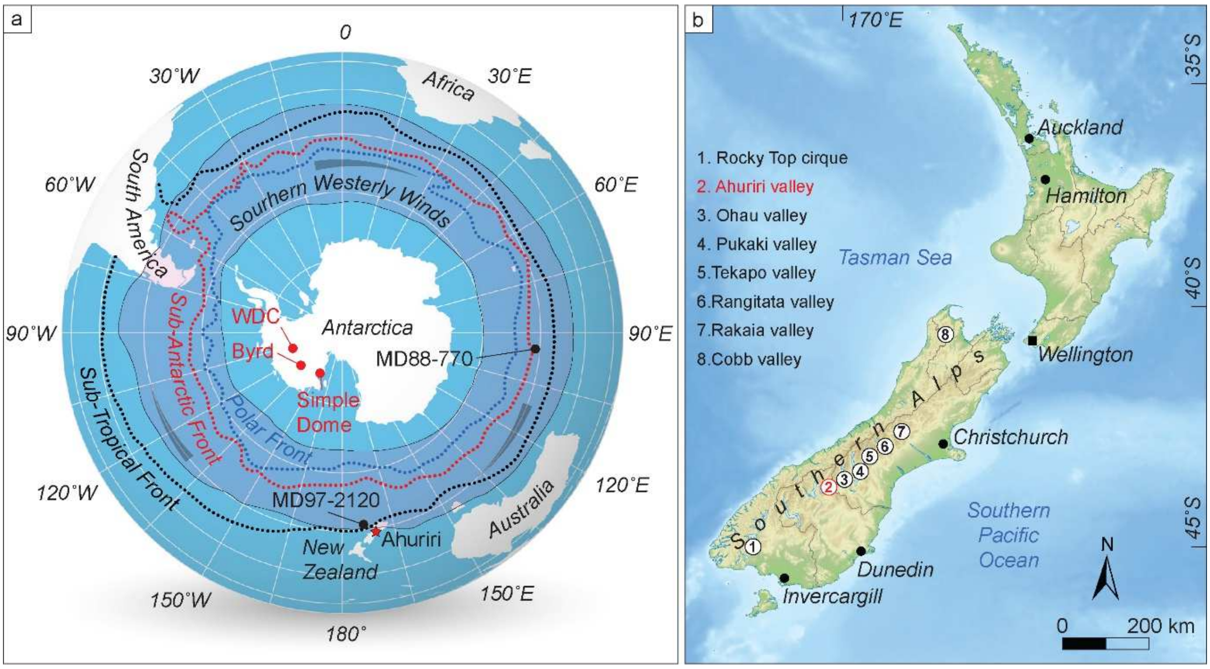

Figure 1. a - Map of the Southern Hemisphere. Light grey - showing the approximate positions of the Southern Westerly Winds (SWW) belt (Sime et al., 2013); Light grey arrows - direction of the SWW belt; The blue dotted line - Polar Front; The red dotted line - Sub-Antarctic Front; The black dotted line - Sub-Tropical Front (Darvill et al., 2016); The red star - location of the Ahuriri River valley; The black dots - locations of key marine core palaeoclimate records illustrated in Figure 8 and mentioned in the text (Pahnke et al., 2003; Barrows et al., 2007); The red dots - locations of key ice core palaeoclimate records mentioned in the text (Pedro et al., 2012; WAIS Divide Project Members, 2013). b - Location map of New Zealand showing all sites mentioned in the text. See Figure 2 for a detailed view of the Ahuriri River valley.

2 Study area

2.1 Southern Alps

The Southern Alps extend approximately 700 km from northeast to southwest along much of the length of New Zealand's South Island. Overall, there are seventeen peaks that exceed 3,000 metres in height, and the range reaches its maximum elevation in its central section around Aoraki/Mount Cook (3,724 m a.s.l.). The Southern Alps have high uplift rate of about 8±3 mm/year in the central section (Norris and Cooper, 2001), along with the major active transcurrent compound of the Alpine Fault (Kamp and Tippett, 1993). Individual ranges of the Southern Alps are separated by glacial valleys, many of which contain glacial lakes.

The Southern Alps lie perpendicular to the prevailing westerly flow of air masses, dividing South Island into strongly different climate regions. The western slopes of the Southern Alps are the wettest (4,000-10,000 mm/year), whereas the eastern slopes are drier (<1,000 mm/year) (Chinn et al., 2014). Mean annual air temperatures range from 9°C to 13°C at sea level across the South Island. The coldest month is usually July and the warmest is January or February. Temperatures decrease at rate of about ~1°C for every 200 m increase in altitude (Norton, 1985) providing low temperature on many mountain summits that are sufficiently cold to enable perennial survival of snow and thus glacierization (Chinn et al., 2014).

Equilibrium line altitudes for glaciers in the Southern Alps vary with latitude (Porter, 1975) (which affects temperature) and west to east precipitation gradients (Lamont et al., 1999), as well as aspect (Carrivick and Chase, 2011). The high precipitation on the west-facing slopes of the Southern Alps sustains glaciers that descend to just a few hundred meters above sea level (Purdie et al., 2014). The largest glaciers and snowfields can be found west of, or straddling, the highest peaks of the main watershed range, with smaller glaciers typically located further east. According to the latest inventory (Baumann et al., 2020), this mountain range contains over 3,000 glaciers with approximately 800 km^2 total area. Tasman Glacier is the largest in New Zealand with ~83 km^2 area.

2.2 Ahuriri River valley

The Ahuriri River originates on the eastern slopes of the central Southern Alps and forms the border between the Canterbury and Otago regions. The river flows approximately 70 km from the north-west (Mt. Huxley 2505 m a.s.l., -44° 4'15.58"S, 169°40'42"E) to the south-east (conjunction with Lake Benmore -44°30'30.18"S, 170° 3'26.51"E), within the Waitaki (Mackenzie) River basin.

Detailed glacial geomorphological mapping of the Ahuriri study site is presented in Tielidze et al. (2021). Our study area includes the upper portion of the Ahuriri River catchment, spanning about 45 km from the headwater (Figure 2). The upper section of the Ahuriri River valley (~20 km from the headwater) surrounded by Huxley (western side) and Barrier (eastern side) ranges and is relatively narrow with steep slopes and high elevation with several peaks exceeding 2200 m a.s.l. Canyon Creek on western valley side, and Watson Stream and Hodgkinson Creek on the eastern side, are the main tributaries of the Ahuriri River in this upper region. In the middle and lower sections, the Ahuriri River valley has very low bed slope (~5 m/km). The bottom of the lower and middle section of the valley contains prominent terminal and lateral (hummocky) moraine systems that were selected for this study, hereafter called moraine belts 3, 2, and 1.

Glacial sequences in the Aruhuri River valley have not been previously dated using modern geochronological methods. Only relative ages based on 1:250,000 geological maps by Turnbull (2000) and Rattenbury et al. (2010) are available. The Ahuriri River basin contains geological formations of the Quaternary age, ranging from the Late Pleistocene to Holocene. The Holocene deposits are characterised by angular, unsorted, blocky rock debris (scree), boulder till, and variable mixtures of rock debris, sand, silt (colluvium), and cirque moraines. Holocene moraines are mainly found in the headwater of the Ahuriri River and its tributaries. The upper section of the valley is characterised by alluvial deposits such as the alluvial plains consisting of gravel, sand, mud and minor peat, while the alluvial fans contain gravel and sand commonly with large boulders from landslides and rockfalls. Late Pleistocene glacial deposits in the middle and lower valley are built by poorly sorted, generally unweathered boulder (greywacke) till with interlayered silt. In the lower section the Ahuriri River bed is cut into the Late Pleistocene (Hawera series) alluvial (including glacial outwash) deposits and tills. Peat swamp deposits with interbedded, mud and gravel are mainly found at the lower section of the valley.

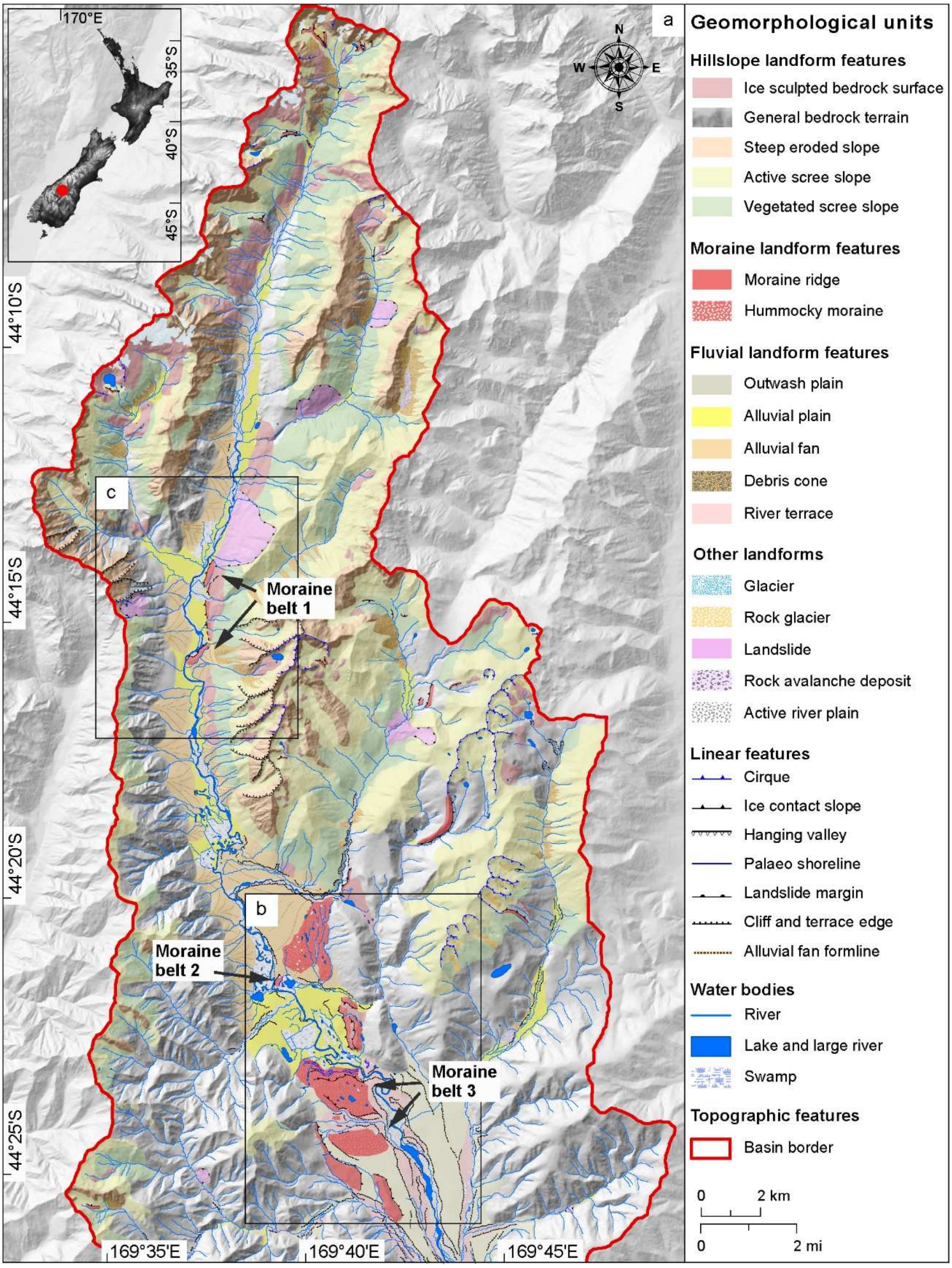

Figure 2. a – Simplified overview map of the glacial geomorphology of the Ahuriri River valley (Tielidze et al., 2021). Study area location is given on regional New Zealand insert map. b – terminal moraine systems selected for this study (moraine belts 3 and 2) along with surrounding area. c – terminal-lateral moraine system (moraine belt-1) in the middle valley along with surrounding area. Detailed glacial geomorphological maps of these panels are shown in Figure 5 and 6.

Based on a regional classification (Williams, 1991) the headwater of Ahuriri River valley is placed in South Island Axial Range's zone, while the rest of the territory belongs to the Canterbury Faulted and Folded Belt zone. There are several active and inactive fault lines in the Ahuriri River basin mainly stretching from north-east to south-west of the catchment (Turnbull 2000; Rattenbury et al., 2010). Areas of younger deposits or landforms in the Ahuriri River valley such as young floodplains and river terraces, accumulating fans of stream sediment at the mouths of valleys, gullies, and steep, eroding mountain or hill slopes, are commonly younger than the most recent fault movements. However, the ice-age landforms, such as outwash terraces, and glacially-sculpted landforms, although youthful in a geological sense, are old enough to have been affected by the most recent active fault and fold movements (Barrell, 2016).

3 Methodology

3.1 Field work

We collected 38 samples from Ahuriri moraine systems in the 2019-2020 austral summer: 11 samples from outer (southern) and 11 samples from inner (northern) portion of moraine belt-3 (Figure 3); 5 samples from moraine belt-2; and 11 samples from moraine belt-1 (Figure 4). We targeted the top central surfaces (sample depths = 1-5 cm) of unmodified greywacke boulders that were deposited within the moraine surface. We preferred large boulders with top surfaces well above the ground (heights provided in Table 1) to minimise the potential of prior cover by sediment. Where only smaller boulders (<50cm high) were present, we collected several samples to analyse the age distribution for any post-depositional impacts. Boulders with steep sloping tops or displaying evidence for post-depositional surface erosion (e.g., fresh-looking surfaces, evidence of human activities etc.) were avoided. Quartz veins were targeted using a portable rock saw, hammer, and chisel. For measuring the location and altitude of individual sample we used the Trimble GeoXH and eTrex 20 Garmin GPS. We measured the angle of the surrounding horizon using a clinometer and geological compass, which were combined with strike and dip observations of each boulder surface to calculate topographic shielding of the cosmic ray flux using the online exposure (formerly known as CRONUS-Earth) calculator (Balco et al., 2008). Each boulder was measured and photographed from several points of view (Figure 3-4). All field observations are given in Table 1.

Figure 3. Sampled boulders from inner (northern) portion of the Ahuriri terminal moraine terrain. Moraine belt-3.

Figure 4. Sampled boulders from prominent terminal/lateral moraine system. Moraine belt-1.

3.2 Laboratory work

Physical and chemical preparation of samples for ^{10}Be dating took place at the Victoria University of Wellington laboratories. The thickness of all the collected samples, relative to the surface, was measured by callipers before jaw-crushing then sieving to isolate the 250-710 µm fraction. Each sample was then repeatedly passed through the Frantz magnetic separator to remove the magnetic minerals from quartz-rich fractions.

Next, three leaching steps were performed: i) twice in a 10% HCl solution for 24 hours each, ii) once in a 5% HF / 1% HNO_3 solution for 24 hours, and finally, iii) twice in a 2.5% HF / 0.5% HNO_3 solution for 48 hours each (Kohl and Nishiizumi, 1992). Samples were rinsed in MQ water and dried down following steps i and iii. A 1008.4 ppm ^{9}Be carrier from University of Melbourne was added to the clean quartz (~280µg ^{9}Be to each sample, Table 1) which was then digested in concentrated HF. Beryllium was isolated using ion exchange chromatography to remove contaminants and $BeOH_2$ was precipitated at pH9 (Ochs and Ivy-Ochs, 1997). All the samples were calcined over a flame, mixed with niobium (Nb) powder at a ratio of 2:3 (BeO:Nb by volume) and packed into stainless steel targets.

3.3 Exposure age calculations

^{10}Be/^{9}Be ratios of all targets were measured by accelerator mass spectrometry at Lawrence Livermore National Laboratory (CA, USA). Samples were measured relative to the 07KNSTD standard (^{10}Be/^{9}Be = 2.85 x 10^{-12}) (Nishiizumi et al., 2007). Moraine exposure ages were calculated using the Macaulay calibration dataset of Putnam et al. (2010). For comparison, we also present ages using the primary global production rate calibration dataset of Borchers et al. (2016). We assumed a rock density of 2.7 g/cm^3 and applied a sample thickness correction for each sample based on laboratory measurements made prior to crushing (Table 1).

Age calculations were carried out using the online exposure (formerly CRONUS-Earth) calculator, version 3 (Balco, 2011). This version calculates exposure ages using the scaling methods: St (Stone, 2000), Lm (Balco et al., 2008), and LSD (Lifton et al., 2014). For consistency with previous studies from the Southern Alps (e.g. Putnam et al., 2013a-b; Strand et al., 2019), our discussion uses results from the Lm scaling method and this scaling decision does not affect our overall conclusions. We used the chi-squared outlier detection routine from the exposure age calculator version 3 (Balco, 2017a, 2017b) to assess if the spread in ^{10}Be exposure ages for a single moraine belt is consistent with a synchronous period of deposition. Furthermore, we follow the calculator documentation regarding presentation of summary ages and uncertainties for each landform (e.g. weighted mean or arithmetic mean; see Balco, 2017a, section 4C).

3.4 Reconstruction of equilibrium line altitude

Detailed glacial geomorphological mapping (e.g., Tielidze et al., 2021) permits delineation of past ice limits and reconstruction of past glacier extent, which is an essential step for calculating palaeo ELAs (Porter, 1975). The accumulation area ratio (AAR) is a straightforward technique for ELA estimation, and has been used for glacier-climate reconstructions in different mountain ranges around the world (e.g., Porter, 2001; Lukas, 2007; Pellitero, 2015) and in New Zealand in particular (e.g., Porter, 1975; Kaplan et al., 2010; Chinn et al., 2012; Putnam et al., 2012; Eaves et al., 2016, 2017). This method assumes that the accumulation area of a glacier occupies a fixed proportion of the total glacier area (Benn and Gemmell, 1997). Knowledge of mass-balance gradients is not required for this method, however, a reconstructed 2D glacier-surface is needed to calculate the AAR.

The lowest terminus limit used in this study is based on our ages from the prominent terminal moraine (belt-3). Other glacier limits (e.g., marginal, headwall) were defined from a detailed glacial geomorphological map (Tielidze et al., 2021) and high-resolution aerial imagery. For the palaeo glacier area uncertainty we used a buffer method which is broadly adopted for modern glacier mapping (e.g., Granshaw and Fountain 2006; Tielidze et al., 2018). A buffer width of 100 m was created along the glacier outline, and the uncertainty term was calculated as an average ratio between the original glacier area and the area with a buffer increment. This generated an average uncertainty of the mapped glaciers area of ±9 %. We manually mapped the past glacier outlines and reconstructed glacier surface contours at 50 m intervals in the 800-1300 m elevation zone and at 100 m intervals in the 1300-2400 m elevation zone. Contour lines were drawn mimicking a typical glacier surface topography (consistent with principles of glacier flow): convex near the terminus, horizontal at mid-elevations, and concave near the headwall. We assume that the largest source of error associated with this method is the reconstruction of glacier surface contours. Nevertheless, this uncertainty is considered to be randomly distributed and unlikely to introduce major deviations (Nesje and Dahl, 2000).

Based on the reconstructed glacier contour lines we created a 30 m resolution digital elevation models (DEMs) in ArcGIS software 10.6.1. The area between each pair of successive contours was measured automatically in ArcGIS by ELA calculation toolbox (Pellitero et al., 2015). Empirical studies of modern glaciers have shown that under steady-state conditions the AAR typically falls between 0.5 and 0.8 meaning that the accumulation area occupies approximately two-thirds of the glacier's total area (Meier and Post, 1962). The AAR of 0.67 with a nominal 1 standard deviation uncertainty of 0.05 is used in this study, which is standard for New Zealand glaciers (Chinn et al., 2012) and the commonly-adopted value for palaeoglacial reconstructions in this region (e.g. Kaplan et al., 2010; Putnam et al., 2012; Eaves et al., 2016, 2017).

In order to reconstruct past temperature conditions (relative to present (1981-2010) (NIWA, 2012)) associated with the palaeo ELA, we translate the magnitude of ELA change, relative to present to temperature change using a temperature lapse rate and assuming no change in precipitation. To reflect the high uncertainty in the key variables for ELA-temperature estimation, Eaves et al. (2016, 2017) employed a Monte-Carlo approach that repeatedly resampled distributions of the present-day ELA and the temperature lapse rate. Here we follow the same approach. To derive estimates of the present-day ELA, we used recently mapped modern glacier outlines from the Ahuriri River valley (Tielidze et al., 2021) along with a medium resolution (15 m) DEM (Columbus et al., 2011) and applied the AAR automatic approach (Pellitero et al., 2015) with the same ratio (0.62-0.72). The present-day temperature lapse rate in New Zealand is ~5°C km^{-1} (Norton, 1985; Tait and Macara, 2014), although it is poorly constrained by observations. Thus, we follow Eaves et al. (2016) in selecting temperature lapse rates from an evenly-distributed range from -4 to -7°C km^{-1}. The algorithm repeatedly resamples these input parameters providing a population of palaeo equilibrium line altitude (*p*ELA) and delta temperature (*d*T) estimates that represent a full window of parameter uncertainty.

4 Results

4.1 Moraine belt-3

A large terminal moraine unit (~3.5 km long and 1.6 km wide) at an elevation of about 760 m a.s.l. was identified in the lower section of the Ahuriri River valley, defining a former ice margin. The surface of this landform is broad and lacks sharp crests, however, it is scattered with large 1 to 2 m (diameter) sized greywacke boulders. The upper surface of the moraine is in some places lined by low, broad ridges that range in height from 1 to 5 metres above the general moraine surface. Two small ponds occur on the surface of this terrain. The middle part of the moraine is incised by a meltwater channel, which divides the moraine into two parts, inner (44° 23′ 54″ S, 169° 39′ 48″ E) and outer (44° 24′ 36″ S, 169° 40′ 25″ E) (Figure 5). The inner (northern) part of the moraine has a hummocky nature and is characterised by relatively shorter, steeper angle up-glacier faces, and longer, low down-glacier faces. Multiple former shorelines (44°23'25"S, 169°39'31"E) at different elevations (~720–740 m a.s.l.) occur on the up-glacier faces of the hummocky moraine belt which likely represents a palaeo lake and its subsequent recession (Tielidze et al., 2021). These shorelines manifest as multiple platforms nested at several elevations (~725, 734, and 740 m a.s.l.) that extend horizontally for between ~50 and ~300 metres. In total, we identified three clear (and several possible) former shorelines running parallel to each other. The outer (southern) section of the moraine belt is more subtle and flat.

Sample details for surface exposure ages from all moraine systems are given in Table 1, while cosmogenic ^{10}Be exposure ages are listed in Table 2. All age calculations are referenced to calendar year before sample collection (2019).

Eleven samples from the inner (northern) part of a moraine belt-3 show individual apparent exposure ages ranging from 17.6±0.4 to 20.9±0.5 ka (Table 2 and Figure 5). The ages from this moraine belt were grouped around an exposure age of 20.1±0.4 ka (n=10; 1 outlier - AL-27-61, see methods for details), based on the internal error-weighted mean of the eleven exposure ages. Eleven exposure ages from the outer (southern) moraine range from 19.1±0.4 to 20.0±0.6 ka (Table 2 and Figure 5). These eleven ages yield internal error-weighted mean age of 19.5±0.4 ka (n=11; no outliers). Because the mean ages of the Ahuriri moraine belt-3 at the inner and outer sites are within error of each other, we interpret this feature as one continuous moraine that formed 19.8±0.3 ka ago. The entire moraine was probably divided by a meltwater channel when the glacier was located nearby. These results suggest that 19.8±0.3 ka ago, the glacier margin was located at the outermost terminal moraine system of the Ahuriri valley at an elevation of ~760 m a.s.l. Overall, a comparison of exposure ages from all the different scaling or calibration models (St, Lm, LSD, and Global) shows that this conclusion is insensitive to the choice of scaling model (Table 2), thus we proceed using the Lm model of Balco et al., (2008).

4.2 Moraine belt-2

Approximately 4 km upstream from moraine belt-3, on the eastern side of the Ahuriri River, we identified a flight of left-lateral moraines that descend in elevation from ~785 m a.s.l on the valley side down to ~710 m a.s.l close to the present-day riverbank. The outermost portion of this sequence grades down-valley to intersect with moraine belt-3, thus we interpret the inner parts of this sequence to represent a recessional sequence that records glacier surface lowering after 19.8±0.3 ka.

We targeted the lowest, innermost section of this moraine sequence for surface exposure dating, to bracket the timing of glacier thinning at this location. Our target moraine is a prominent, isolated moraine hummock situated immediately adjacent (east of) the present-day Ahuriri River at the edge of largest alluvial fan in the middle-lower section of Ahuriri River valley (Figure 5) (44°21'46"S, 169°38'15"E). A single former shoreline at elevation of 721 m a.s.l. occurs on the outer face of this moraine belt, which likely represents a subsequent recession of a palaeo lake. The surroundings of the moraine belt are swampy with several small ponds. Several greywacke boulders are embedded in the slopes and crest of the moraine, ranging in elevation between 720-740 m a.s.l.

Five samples from moraine belt-2 range from 9.9±0.3 to 12.2±0.5 ka (Table 2 and Figure 5). The ages from this moraine belt were grouped around an exposure age of 11.3±0.7 ka (n=4; 1 outlier - AML-28-105), based on the internal error-weighted mean of the five exposure ages. Although these ages are morphostratigraphically consistent with moraine belt-3, they are unusually young for their situation in the lower valley and are inconsistent in age relative to moraine belt-1 below. As such, we do not believe these ages represent the timing of deposition by ice and we discuss the possible reasons for this discrepancy in the discussion (section 5.2.1), below.

4.3 Moraine belt-1

Approximately 11.5 km upstream from moraine belt-2, a prominent terminal-lateral moraine system extends for approximately 4 km in the middle section of the Ahuriri River valley between 760 and 800 m a.s.l. (Figure 6) (44°15'44"S, 169°36'41"E). The middle section of this moraine is linear, while the lower section is curvilinear and demarcates the limits of former glacier margin. This feature comprises fragmentary crested ridges (divided by meltwater channels or river streams) exhibiting ~30 m relief from the present valley floor and usually up to a few hundred metres long. The surface of upstream section of the moraine terrain is broad and exhibits distinct ridge crests. Here ice-moulded bedrock ridges, streamlined in the former direction of ice flow, protrude through the overlying moraine. Large sized (1 to 2 m diameter) greywacke boulders are found in many places on the crest of the fragmented moraine ridges. We collected samples from a mixture of erratic boulders (n=6) and ice-moulded bedrock surfaces (n=5).

Six ages from the boulders of moraine belt-1 are tightly clustered and range from 16.6±0.4 to 17.1±0.4 ka (Table 2 and Figure 6). The ages from these boulders were grouped around an error-weighted mean exposure age of 16.7±0.3 ka (n=6; no outliers). Five exposure ages from the bedrock surfaces of moraine belt-1 range from 16.3±0.4 to 16.8±0.4 ka (Table 2 and Figure 6). These five ages yield internal error-weighted mean age of 16.6±0.3 ka (n=5; no outliers).

Our ages from the boulders, which are situated on the moraine ridge crests, represent the final stages of moraine formation. Meanwhile, the bedrock ages record the withdrawal of ice and onset of bedrock exposure. As the two sample populations date complementary events in the glacier history, we expect them to be similar in age. As this is the case, we consider a combined age 16.7±0.3 ka to best represent the culmination of moraine building and withdrawal of ice from this site.

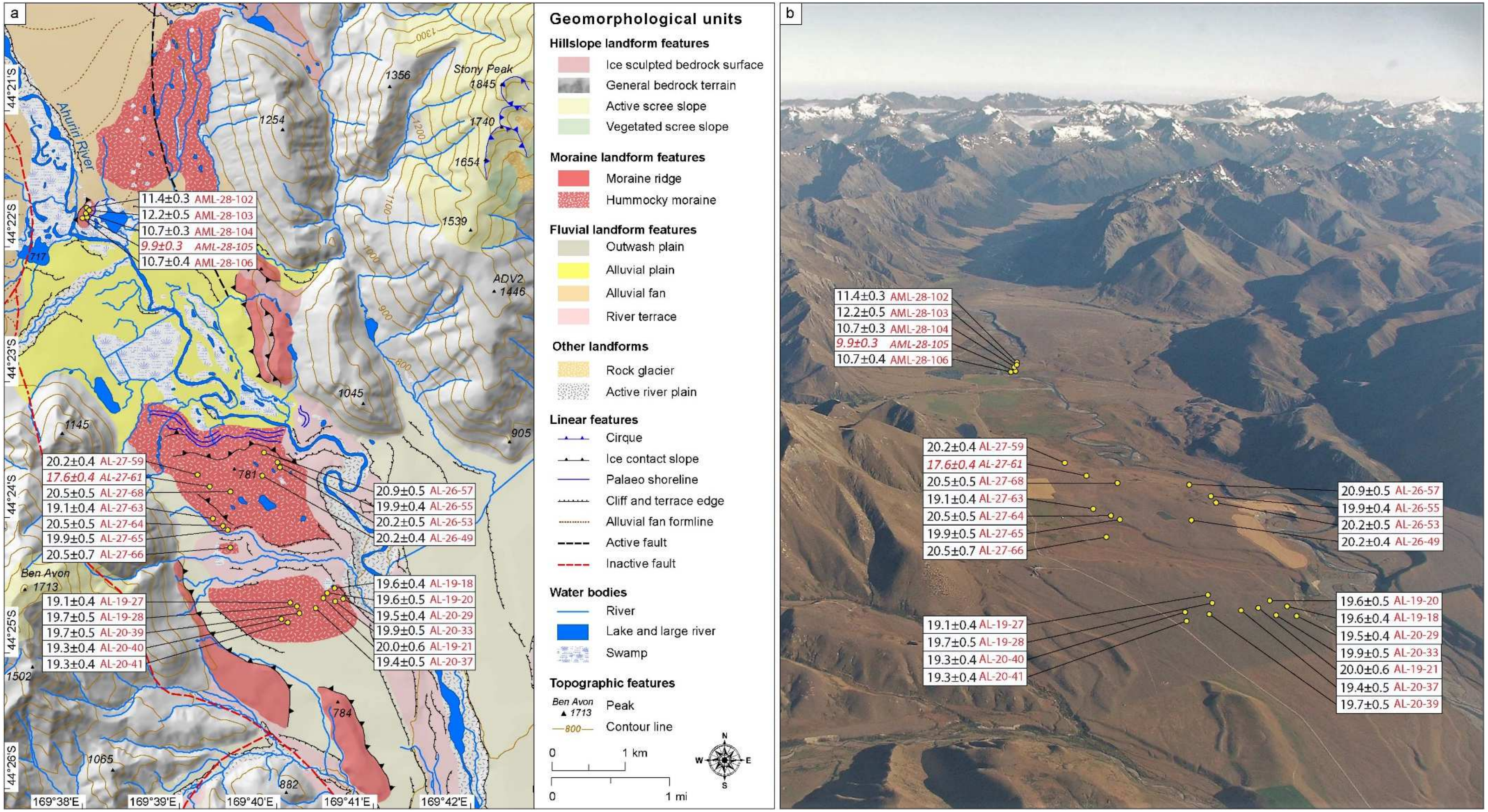

Figure 5. a – Glacial geomorphological map of the Ahuriri terminal moraine systems (moraine belts 3 and 2) and surrounding area described in this study. See Figure 2 for map location with respect to the Ahuriri River valley. b – Oblique aerial view of the Ahuriri River valley from south to north (Photo by K. Norton). Yellow dots on both panels indicate the location of the samples (see Table 1-2 for more details). The outlier samples are given by red italic text (see discussion section below).

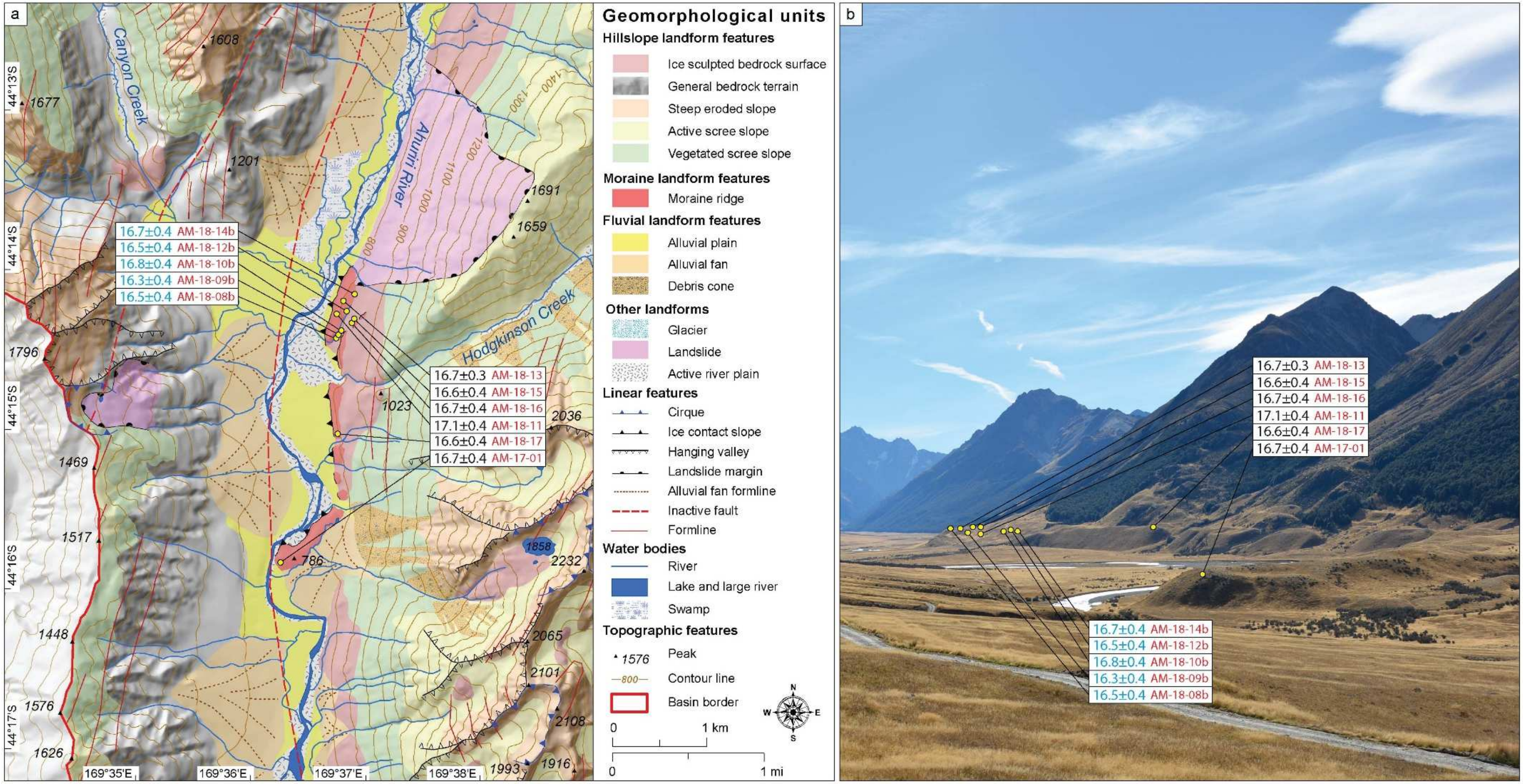

Figure 6. a – Glacial geomorphological map of the Ahuriri terminal moraine system (moraine belt-1) and surrounding area. See Figure 2 for map location with respect to the Ahuriri River valley. b – Field photo of the Ahuriri moraine belt-1 (by L. Tielidze). Yellow dots on both panels indicate the location of the samples (see Table 1-2 for more details). The black ages are from boulders while the blue ages are from bedrock.

Table 1. Surface-exposure sample details and ^{10}Be data of moraine systems from the Ahuriri River valley. Italic ages indicate outliers that were excluded from the chi-squared test (Balco, 2017a, 2017b). See Table 2 for the extracted ages and Figure 5-6 for sample location.

Sample field ID	LLNL ID	Boulder/ Bedrock	Latitude (S)	Longitude (E)	Elevation (m a.s.l.)	Boulder size (L×W×H) (cm)	Sample thickness (average cm)	Shielding correction	Quartz weight (g)	Carrier (^{9}Be) added (g)	^{10}Be/^{9}Be ± 1σ (10^{-14})	[^{10}Be] ± 1σ (10^4) (atoms/gram qtz.)
Moraine belt-3 (inner) (44°23′54″S, 169°39′48″E)												
AL-26-49	BE48600	Boulder	-44.395441	169.666723	774	170×140×95	2.3	0.998195	13.3375	0.2814	11.20±0.21	15.82±0.35
AL-26-53	BE48601	Boulder	-44.393977	169.669205	774	180×95×80	4.0	0.990586	13.5432	0.2823	11.11±0.21	15.50±0.35
AL-26-55	BE48602	Boulder	-44.393104	169.668986	768	240×228×78	2.8	0.993362	13.3095	0.2841	10.76±0.20	15.37±0.34
AL-26-57	BE48603	Boulder	-44.391977	169.666613	765	300×280×150	2.8	0.998693	13.6803	0.2836	11.64±0.22	16.16±0.36
AL-27-59	BE48604	Boulder	-44.394375	169.655063	769	144×138×36	1.7	0.996929	13.6810	0.2851	11.32±0.21	15.79±0.35
AL-27-61	*BE48605*	Boulder	*-44.395731*	*169.658087*	*766*	*211×110×24*	*2.4*	*0.998627*	*13.1517*	*0.2827*	*9.48±0.18*	*13.62±0.30*
AL-27-63	BE48606	Boulder	-44.400109	169.657308	767	332×150×64	2.4	0.995922	12.7456	0.2850	9.91±0.18	14.82±0.32
AL-27-64	BE48607	Boulder	-44.401301	169.659033	769	268×262×171	2.5	0.992318	13.5983	0.2822	11.43±0.21	15.88±0.35
AL-27-65	BE48608	Boulder	-44.401771	169.659769	769	157×102×67	2.7	0.998846	13.4261	0.2840	10.91±0.21	15.45±0.35
AL-27-66	BE48609	Boulder	-44.403993	169.659257	774	420×350×130	2.8	0.995555	12.9888	0.2835	10.91±0.33	15.93±0.52
AL-27-68	BE48610	Boulder	-44.396934	169.660573	768	182×147×69	3.8	0.991419	12.8317	0.2839	10.60±0.21	15.69±0.35
Blank	BE48611	-	-	-	-	-	-	-	-	0.2747	0.08±0.02	-
Moraine belt-3 (outer) (44°24′36″S, 169°40′25″E)												
AL-19-18	BE48481	Boulder	-44.409645	169.678879	757	160×110×60	1.9	0.990779	11.6167	0.2760	9.81±0.17	15.08±0.33

AL-19-20	BE48482	Boulder	-44.410053	169.677258	759	201×171×81	2.0	0.998955	12.1344	0.2757	10.29±0.22	15.15±0.39
AL-19-21	BE48483	Boulder	-44.410519	169.677116	759	244×144×90	2.3	0.998955	13.3596	0.2762	11.51±0.29	15.49±0.45
AL-19-27	BE48484	Boulder	-44.41137	169.67104	761	163×132×65	2.7	0.998955	15.1612	0.2758	12.44±0.23	14.77±0.33
AL-19-28	BE48485	Boulder	-44.41184	169.67271	757	266×127×57	4.3	0.998955	13.7932	0.2784	11.38±0.24	14.95±0.37
AL-20-29	BE48486	Boulder	-44.41072	169.68034	753	251×210×138	2.1	0.998955	14.6778	0.2782	12.17±0.23	15.05±0.34
AL-20-33	BE48487	Boulder	-44.41117	169.67877	762	357×173×170	2.0	0.974704	14.5035	0.2714	12.35±0.25	15.07±0.36
AL-20-37	BE48488	Boulder	-44.41179	169.67583	755	207×184×80	2.9	0.998955	14.1247	0.2766	11.65±0.22	14.86±0.35
AL-20-39	BE48489	Boulder	-44.41282	169.67349	756	182×133×55	2.3	0.998680	14.3993	0.2775	12.10±0.23	15.21±0.35
AL-20-40	BE48490	Boulder	-44.41389	169.6703	758	443×365×66	2.6	0.998955	14.0415	0.2752	11.65±0.22	14.87±0.34
AL-20-41	BE48491	Boulder	-44.41443	169.6712	753	112×98×41	2.1	0.976371	15.1486	0.2787	12.14±0.21	14.57±0.32
Blank	BE48492	-	-	-	-	-	-	-	-	0.2737	0.4±0.04	-
Moraine belt-2 (44°21′46″S, 169°38′15″E)												
AML-28-102	BE49454	Boulder	-44.362613	169.637987	738	150×130×40	1.1	0.996832	13.5616	0.2772	6.47±0.16	8.55±0.24
AML-28-103	BE49455	Boulder	-44.362858	169.637718	738	200×160×70	4.1	0.994472	7.7271	0.2782	3.95±0.14	8.96±0.36
AML-28-104	BE49456	Boulder	-44.363229	169.637915	736	110×80×40	2.2	0.994472	14.1598	0.2789	6.25±0.14	7.95±0.21
AML-28-105	*BE49457*	Boulder	*-44.363044*	*169.637183*	*731*	*130×90×80*	*2.6*	*0.992993*	*14.0255*	*0.2793*	*5.64±0.14*	*7.22±0.20*
AML-28-106	BE49458	Boulder	-44.362497	169.637083	727	120×100×70	3.0	0.997196	13.5082	0.2794	5.87±0.18	7.82±0.27
Blank	BE49459	-	-	-	-	-	-	-	-	0.2754	0.3±0.04	-
Moraine belt-1 (Boulders) (44°15′44″S, 169°36′41″E)												
AM-17-01	BE47757	Boulder	-44.264579	169.605771	775	185×90×156	1.1	0.927932	15.1732	0.2991	9.35±0.16	12.23±0.30
AM-18-11	BE47761	Boulder	-44.241326	169.614783	800	231×145×110	1.4	0.984798	16.7197	0.2987	11.46±0.26	13.52±0.35

AM-18-13	BE47763	Boulder	-44.239497	169.616435	813	172×131×65	1.3	0.986981	13.7934	0.2949	9.56±0.15	13.39±0.27
AM-18-15	BE47765	Boulder	-44.239671	169.619302	863	75×50×48	0.9	0.976531	15.4166	0.2951	10.87±0.21	13.71±0.32
AM-18-16	BE47766	Boulder	-44.239705	169.619328	863	97×75×45	0.9	0.969833	12.9430	0.2941	9.25±0.17	13.74±0.31
AM-18-17	BE47767	Boulder	-44.25119	169.61516	804	320×175×80	2.6	0.979546	15.6424	0.2908	10.60±0.20	12.93±0.29
Moraine belt-1 (Bedrock) (44°15′44″S, 169°36′41″E)												
AM-18-08b	BE47758	Bedrock	-44.241709	169.614529	798	Bedrock	1.6	0.988486	15.5916	0.2980	10.38±0.19	13.04±0.29
AM-18-09b	BE47759	Bedrock	-44.241693	169.614466	798	Bedrock	1.6	0.981724	15.3914	0.2969	10.13±0.19	12.77±0.29
AM-18-10b	BE47760	Bedrock	-44.241688	169.61446	797	Bedrock	2.5	0.944171	15.4690	0.2977	10.02±0.19	12.62±0.29
AM-18-12b	BE47762	Bedrock	-44.241384	169.614766	800	Bedrock	1.2	0.991202	16.8167	0.2972	11.28±0.21	13.13±0.30
AM-18-14b	BE47764	Bedrock	-44.23724	169.617903	820	Bedrock	1.3	0.985638	16.2337	0.3289	10.08±0.19	13.45±0.30
Blank	BE47768	-	-	-	-	-	-	-	-	0.2977	0.3±0.03	-

Table 2. Cosmogenic ^{10}Be exposure ages (with internal 1-sigma uncertainties) from the moraine belts in the Ahuriri River valley. Three scaling schemes: St (Stone, 2000), Lm (Balco et al., 2008), LSD (Lifton et al., 2014) and the "Macaulay" production rate (Putnam et al. 2010) was used for exposure age calculations. Ages calculated using a global production rate (Borchers et al., 2016) are also presented without external uncertainties that are much higher due to the large uncertainties in the global ^{10}Be production rate calibration dataset. Italic ages indicate outliers that were excluded from the chi-squared test (Balco, 2017a, 2017b).

Sample field ID	St age (ka) and internal uncertainty	**Lm age (ka) and internal uncertainty**	LSDn age (ka) and internal uncertainty	Lm age (ka) and internal uncertainty Global prod. rate
Moraine belt-3 (inner) (44°23′54″S, 169°39′48″E)				
AL-26-49	20924±464	**20204±448**	20032±444	19272±427
AL-26-53	20963±469	**20241±453**	20068±449	19307±432
AL-26-55	20604±458	**19906±442**	19747±438	18987±421
AL-26-57	21631±479	**20859±462**	20679±458	19899±441
AL-27-59	20896±463	**20178±447**	20010±443	19246±426
AL-27-61	*18118±403*	***17569±391***	*17463±389*	*16752±373*
AL-27-63	19781±424	**19138±410**	18998±407	18250±391
AL-27-64	21255±469	**20512±453**	20336±449	19567±432
AL-27-65	20561±467	**19866±451**	19706±447	18948±430
AL-27-66	21226±701	**20485±677**	20305±671	19541±645
AL-27-68	21258±483	**20515±466**	20341±462	19570±444
Error-weighted mean (n=10)	20859±151 (360)	**20144±146 (350)**	19977±144 (340)	19214±139 (913)
Moraine belt-3 (outer) (44°24′36″S, 169°40′25″E)				
AL-19-18	20312±450	**19636±435**	19491±431	18727±414
AL-19-20	20228±524	**19558±506**	19413±503	18652±483
AL-19-21	20729±606	**20025±585**	19868±580	19100±558
AL-19-27	19772±450	**19131±435**	18994±432	18243±415
AL-19-28	20352±508	**19674±491**	19527±487	18763±468
AL-20-29	20194±463	**19526±448**	19386±444	18621±427
AL-20-33	20563±499	**19869±482**	19714±478	18951±460
AL-20-37	20037±470	**19380±454**	19242±451	18482±433
AL-20-39	20413±468	**19730±452**	19584±449	18818±431

AL-20-40	19962±459	**19309±444**	19170±441	18414±423
AL-20-41	20003±436	**19348±422**	19212±419	18451±402
Error-weighted mean (n=11)	20201±144 (348)	**19533±140 (338)**	19390±139 (330)	18628±133 (885)
All samples error-weighted mean (n=21)	20516±104 (338)	**19826±101 (329)**	19672±100 (319)	18909±96 (893)
Moraine belt-2 (44°21′46″S, 169°38′15″E)				
AML-28-102	11538±326	**11391±322**	11446±324	10860±307
AML-28-103	12423±509	**12204±500**	12228±501	11665±478
AML-28-104	10864±293	**10747±290**	10798±291	10267±277
AML-28-105	*9958±287*	***9904±285***	*9977±288*	*9462*±273
AML-28-106	10799±380	**10688±376**	10742±378	10208±359
Error-weighted mean (n=4)	11406±756 (777)	**11258±707 (729)**	11304±695 (716)	10750±677 (844)
Moraine belt-1 (Boulders) (44°15′44″S, 169°36′41″E)				
AM-17-01	17233±419	**16730±406**	16646±404	15946±387
AM-18-11	17639±455	**17115±442**	17013±439	16314±421
AM-18-13	17238±355	**16733±344**	16623±342	15948±328
AM-18-15	17054±399	**16551±388**	16414±384	15777±369
AM-18-16	17224±392	**16717±381**	16568±377	15933±363
AM-18-17	17071±390	**16570±379**	16472±377	15795±361
Error-weighted mean (n=6)	17226±163 (315)	**16720±158 (307)**	16606±157 (300)	15937±150 (763)
Moraine belt-1 (Bedrocks) (44°15′44″S, 169°36′41″E)				
AM-18-08b	17007±386	**16510±374**	16419±372	15737±357
AM-18-09b	16775±383	**16295±372**	16210±370	15528±355
AM-18-10b	17352±395	**16844±383**	16746±381	16056±365
AM-18-12b	17002±384	**16506±373**	16414±371	15733±356
AM-18-14b	17241±389	**16736±378**	16620±375	15950±360
Error-weighted mean (n=5)	17071±173 (318)	**16574±168 (311)**	16478±167 (304)	15797±160 (758)
All samples	17154±119 (293)	**16652±115 (287)**	16546±114 (279)	15871±110 (753)

error-weighted mean (n=11)				

4.5 Palaeo glacier geometry

Based on recent geomorphological mapping (Tielidze et al., 2021), a 15 m DEM (Columbus et al., 2011), high-resolution aerial imagery, and oblique aerial photographs we reconstructed the approximate area and thickness of the palaeo glacier occupying the Ahuriri River valley. According to this calculation, the former glacier covered at least 219±18 km^2 at 19.8±0.3 ka (Figure 7a). The length of the main trunk of the ice (from headwater of the valley to the moraine belt-3) was ~41 km. Canyon Creek was the only large tributary that flowed into the former glacier from the western (right) side, while three large tributaries (Watson Stream, Hodgkinson Stream, and Snowy Gorge Creek) joined the glacier from the eastern (left) side.

The main trunk of the Ahuriri Glacier was relatively narrow (1.5 km) in its upper section. By the middle section, the former glacier doubled in width (~3.0 km), and in its lowest sections, its width was much expanded (~4.0 km) (Figure 7b). The palaeo glacier had also a very low surface inclination in its lower section.

According to our three different profiles, the thickness of the palaeo glacier was at least ~450 m in the upper section, ~350 m in the middle section, and ~300 m in the lower section (Figure 7c). We note that our ice thickness estimate was produced based on modern and manually reconstructed DEMs and it does not consider post-glacial changes in the valley profile resulting from sediment fill. It is likely that the sediment-cover was thinner and the valley floor lower during the glacial period relative to today, thus our ice thickness estimates are likely minimum constraints. However, this uncertainty is irrelevant for equilibrium line altitude reconstruction.

Our reconstructions indicate that glacier area decreased significantly between 19.8±0.3 and 16.7±0.3 ka. The estimated area of all separated ice bodies for 16.7±0.3 ka was 117±15 km^2, while the area of single Ahuriri Glacier was 86±8 km^2 (Figure 8). This indicates that ~18 km (or ~580 m/0.1 ka) of terminus retreat of the palaeo Ahuriri Glacier occurred between 19.8±0.3 and 16.7±0.3 ka.

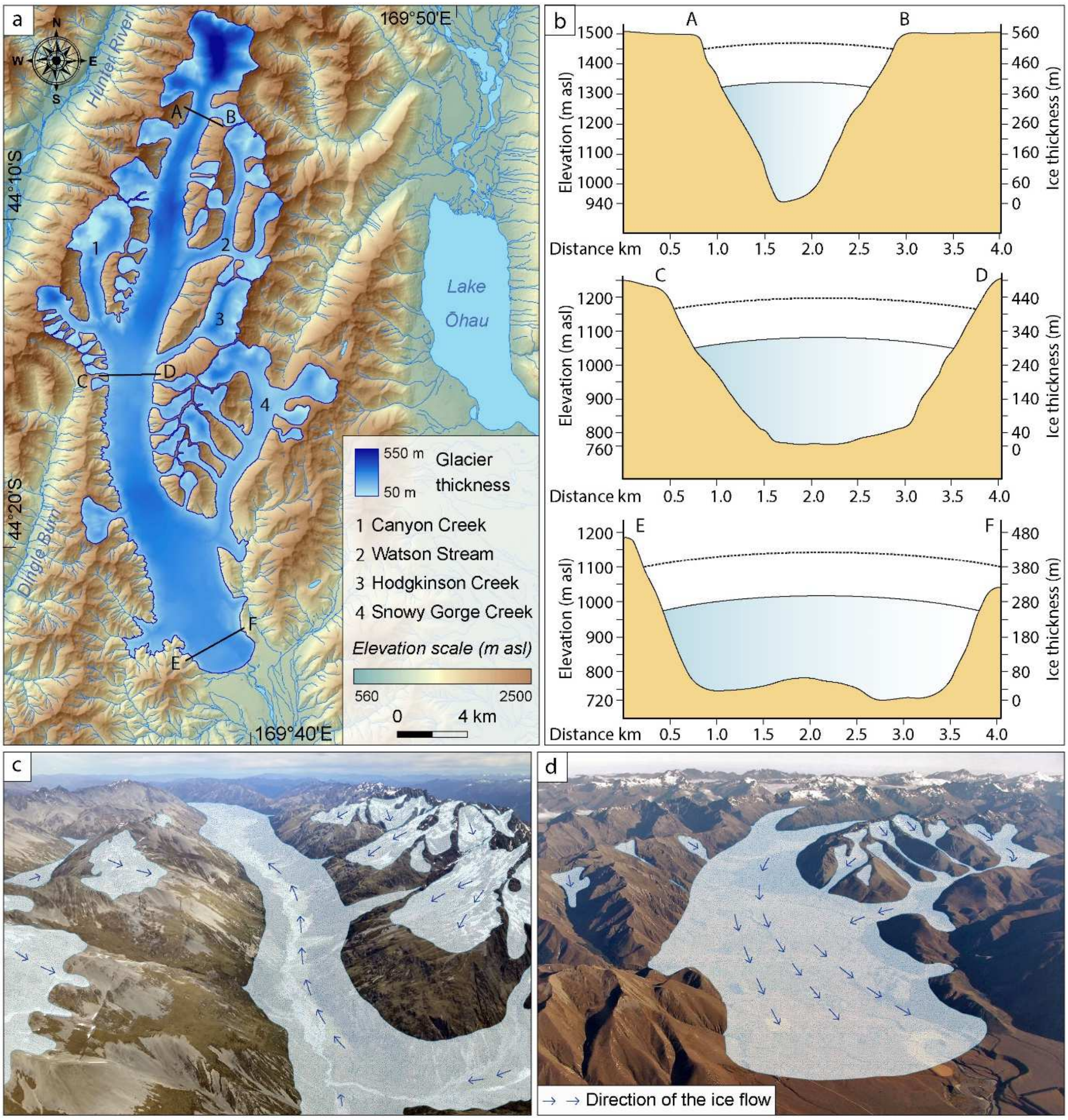

405

406 **Figure 7**. a – Manually derived palaeo Ahuriri Glacier at 19.8±0.3 ka. b – reconstructed ice thickness based on three cross-sections in the lower, middle, and upper sections of the glacier at 19.8±0.3 ka. The black dotted lines show the maximum height that ice could have for that time. Oblique imagery and GIS simulation show palaeo glacier expansion in the upper (c – view from north to south) and lower (d – view from south to north) valley (photos by: W. Dickinson and K. Norton).

411

412 ## 4.6 Palaeo ELA and air temperature

413 Uncertainties in the knowledge of former ice geometries affect the accuracy of reconstructed ELAs for any particular glacier. Our manually reconstructed palaeo Ahuriri glaciers are shown in Figure 8.

Using an AAR of 0.67, we estimate the modern ELA (*m*ELA) at 2000 a.s.l. for the Ahuriri catchment, while the palaeo ELAs (*p*ELAs) are estimated at 1120 m a.s.l. and 1230 m a.s.l, for 19.8±0.3 ka and 16.7±0.3 ka, respectively. This calculation represents an ELA lowering relative to present (*d*ELA) of 880 m and 770 m for 19.8±0.3 ka and 16.7±0.3 ka, respectively. Altering the AAR by ±0.05 (0.62–0.72) yields *p*ELAs of 1170–1060 m a.s.l. for the 19.8±0.3 ka glacier, which represent *d*ELAs of 830–940 m. Similarly, altering the AAR by ±0.05 (0.62–0.72) yields *p*ELAs of 1280–1170 m a.s.l. for the 16.7±0.3 ka glacier, which represents *d*ELAs of 720–830 m.

The temperature lapse rate at the Last Glacial Maximum is not known, and hence we use a range of lapse rate values to estimate the temperature lowering that equates to the *d*ELA. The mean annual temperature lapse rate for upland (>300 m) New Zealand (-5.1°C km^{-1}; Norton, 1985) gives us temperature lowering of -4.5°C and -3.9°C relative to present for the ELA depression of 880 and 770 m for 19.8±0.3 ka and 16.7±0.3 ka respectively. A standard environmental lapse rate (-6.5°C km^{-1}) increases the temperature depression to -5.7°C and -5.0°C for the same times relative to present.

Using a Monte Carlo technique (Eaves et al., 2016, 2017) to combine uncertainties in each variable (*m*ELA, *p*ELA, AAR, and temperature lapse rate), we derive an estimated temperature anomaly of -5.0±1.0°C (1σ) relative to present for 19.8±0.3 ka and -4.4±0.9°C (1σ) relative to present for 16.7±0.3 ka (Figure 8e, h).

433 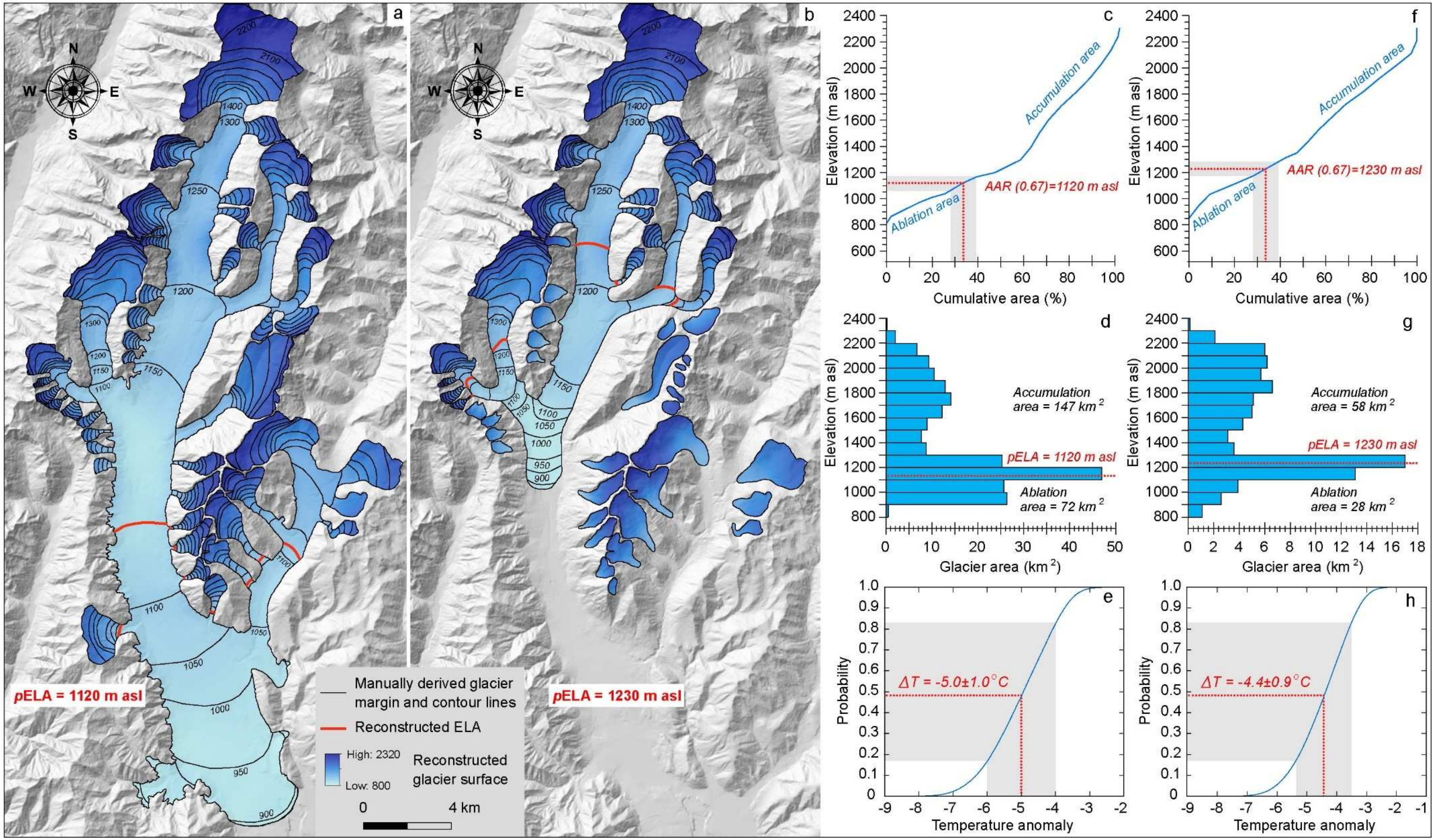

a
b
c
d
e
f
g
h
N
S
W
E
pELA = 1120 m asl
pELA = 1230 m asl
Manually derived glacier margin and contour lines
Reconstructed ELA
High: 2320
Low: 800
Reconstructed glacier surface
0
4 km
Accumulation area
Ablation area
AAR (0.67)=1120 m asl
AAR (0.67)=1230 m asl
Elevation (m asl)
Cumulative area (%)
Accumulation area = 147 km 2
Ablation area = 72 km 2
Accumulation area = 58 km 2
Ablation area = 28 km 2
pELA = 1120 m asl
pELA = 1230 m asl
Glacier area (km 2)
Probability
ΔT = -5.0±1.0°C
ΔT = -4.4±0.9°C
Temperature anomaly

Figure 8. Reconstructed surface of the palaeo Ahuriri Glacier (based on manually derived contour lines) and reconstructed ELA (AAR=0.67) for 19.8±0.3 ka (a) and 16.7±0.3 ka (b). Cumulative curve (surface profile) of the palaeo Ahuriri Glacier for 19.8±0.3 ka (c) and 16.7±0.3 ka (f). The palaeo ELA is shown by the dashed line and shaded box. Hypsometry and reconstructed ELA of palaeo Ahuriri Glacier for 19.8±0.3 ka (d) and 16.7±0.3 ka (g). Cumulative distribution function for the palaeo temperature estimate associated with the Ahuriri terminal moraines for 19.8±0.3 ka (e) and 16.7±0.3 ka (h). Shaded box defines the 1-sigma uncertainty interval[1].

[1] The extent of separate ice bodies on panel "b" is theoretical, as we did not extract any ages at these sites. Therefore, these are not included in the ELA measurements. i.e. the panels "f", "g", and "h", in the figure 8, are created based on a single Ahuriri Glacier (without separate ice bodies).

5 Discussion

5.1 Last Glacial Maximum

Our exposure age data from moraine belt-3 provide robust constraint on the timing of maximum glacier advance during the Last Glacial Maximum in the Arhuriri River valley. Given the ~2.5 km spread of the terminal morainal sequence at moraine belt-3, we anticipated that this landform may have accumulated during several glacial advance events, perhaps across several millennia. However, with the exception of one anomalously young sample, there is no significant difference in boulder ages across this landform within age uncertainties (Figure 5, Table 2). We thus conclude that this moraine formed during a single glacial advance or stillstand and we combine the ages to give the timing of moraine formation as 19.8±0.3 ka. The absence of any older ages from the outer parts of this landform suggests that the largest advance of the last glacial cycle in the Ahuriri valley occurred at ~20 ka, at the height of the global Last Glacial Maximum (Clark et al., 2009).

Comparison of our new data with proximal moraine exposure chronologies shows that the timing of this glacier advance in the Ahuriri valley is consistent with other published ^{10}Be data from the left-lateral moraine system at Lake Pukaki, situated ~60 km to the northeast of our study site. There, a prominent portion of the Mt. John moraine formation is robustly dated to 20.3±0.6 ka (Doughty et al., 2015) and 20.0±0.5 ka (Strand et al., 2019) (Figure 9), which is indistinguishable within uncertainties from the Ahuriri moraine belt-3. However, while the 20-ka advance in the Ahuriri valley represents the largest of the last glacial cycle, the geomorphic records at Lake Pukaki and other nearby sites (e.g. Putnam et al., 2013a) record a much richer history of earlier, slightly more extensive glacier advances spanning much of oxygen isotope stages 2-3 (Denton et al., 2021). Differences in moraine presence between Ahuriri and the Pukaki/Ōhau records are unlikely to be attributable to large scale climatic forcing, given the proximity of all sites to one another. Instead we consider these differences arise from the local topographic settings, which may influence both glacier response to climate (e.g. response times, and length sensitivity), as well as moraine preservation potential. For example, several studies have noted the potential feedback effect of subglacial erosion as a modulator of glacier length in the Pukaki catchment, whereby the large temperate glaciers advancing over and eroding thick packages of unconsolidated sediment may decrease bed elevation and reduce glacier length over time (McKinnon et al., 2012), thus enhancing the preservation potential of older moraines (Barr and Lovell, 2014). There is limited scope for such feedbacks in the Ahuriri valley, where sediment fluxes are lower, and the low surface gradient of the former glacier (Figure 8a) restricted ice velocity, thus increasing the potential for obliterative overlap of moraines by successive glacier advances (Gibbons et al., 1984; Kirkbride and Brazier, 1998).

Despite lower potential for preserving moraines from glacial advances of similar extent, the prominent terminal moraine (moraine belt-3) in Ahuriri does afford clear delineation of past ice extent, which permitted 2D reconstruction of the former ice mass.

Our constraint from moraine belt-3 is in good agreement with glacier chronologies from southern mid-latitudes of South America (Patagonia) (Kaplan et al., 2008; García et al., 2019; Leger et al., 2021) and Australia (Tasmania and Mt Kosciusko) (Barrows et al., 2002; Kiernan et al., 2004; Mackintosh et al., 2006) that indicate glacier advance at ~20 ka.

Using the AAR method, we estimated *p*ELA depression of 830–940 m for the former Ahuriri Glacier at ~19.8±0.3 ka. Porter (1975) also used AAR method (0.6±0.05 ratio) for *p*ELA estimation during the Last Glacial Maximum in the Lake Pukaki drainage basin, and suggested that *p*ELA was 875 m lower during construction of the equivalent Mt. John formation (26.5-18.0 ka; Barrell and Read, 2014). In addition, a glacier modelling simulation by Golledge et al. (2012) indicated that the Last Glacial Maximum ELA was depressed by 800 m (Ōhau, Tekapo glaciers) to 875 m (Pukaki Glacier), consistent with our *p*ELA calculations. Furthermore, modelling experiments by Putnam et al. (2013a) indicate snowline lowering of 920±50 m relative to present since the Last Glacial Maximum at the palaeo Ōhau Glacier.

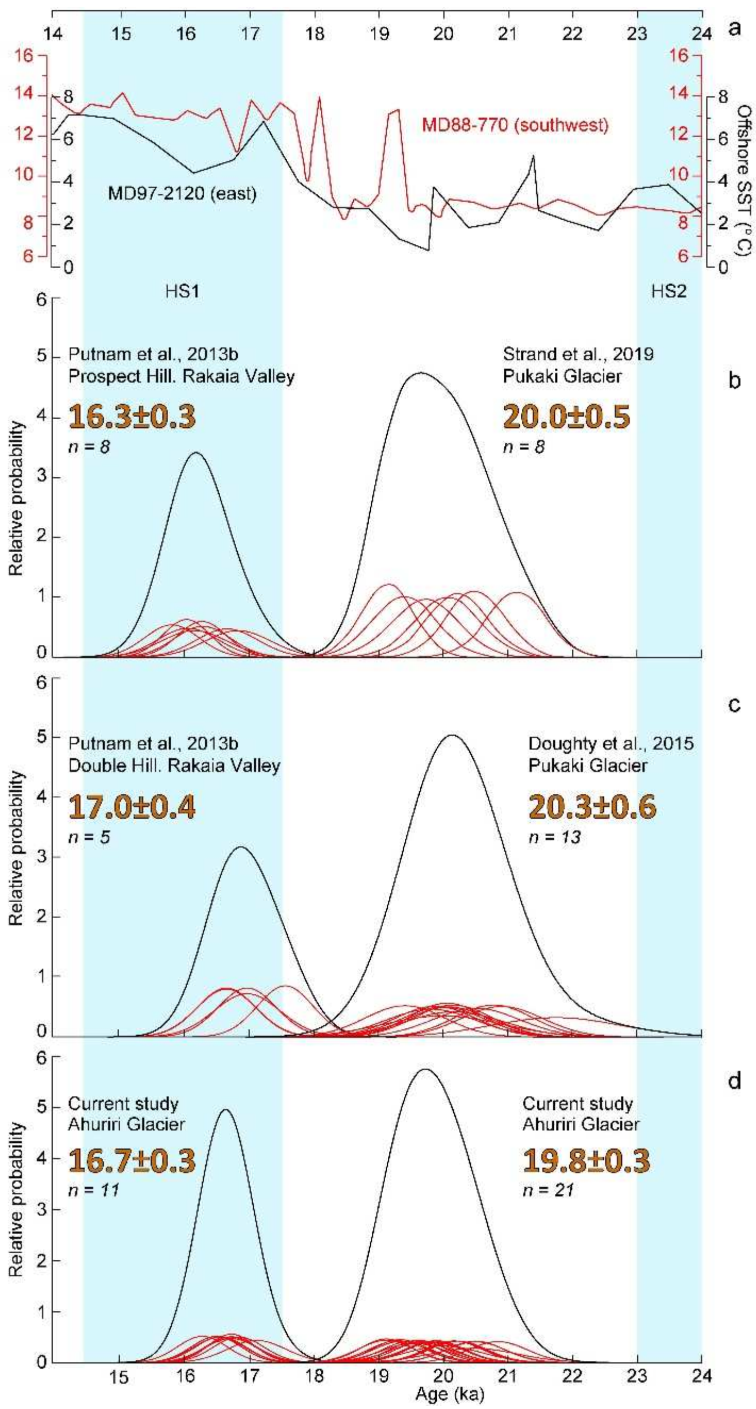

493

494 **Figure 9**. a – Southern Ocean sea-surface temperature (SST) records for 24-14 ka: black - fauna based sediment cores MD88-770 (Barrows et al., 2007); red - Mg/Ca sediment cores MD97-2120 (Pahnke et al., 2003). See also Figure 1 for the location of the coring sites. b-c – A normal kernel density plots or “camel plots” from Pukaki and Rakaia glaciers (Putnam et al., 2013b; Doughty et al., 2015; Strand et al., 2019). d – Ahuriri terminal moraine belts (1 and 3). Outlier sample from current study camel plot was excluded. Blue bands correspond to Heinrich Stadials 1 (HS1) and 2 (HS2).

500

Good agreement was found in the reconstruction of palaeo temperature between the manual and Monte Carlo method in our study. Both methods indicate that local temperature was 5±1°C lower than present when the Ahuriri moraine belt-3 was formed (19.8±0.3 ka). This finding is consistent with modelling studies indicating the Last Glacial Maximum (24-21 ka) temperature depression of 5.8°C below to the modern values from the Cobb valley (e.g., Eaves et al., 2019) or 5.8±0.6°C from Fiordland in 19-17 ka time interval (e.g., Moore et al., 2022). However, while our finding agrees within uncertainty with modelling studies indicating the Last Glacial Maximum temperature depression of 6.25±0.5°C below to the modern values from the Lake Ōhau (e.g., Putnam et al., 2013a) or 6-6.5°C from the entire Southern Alps (e.g., Golledge et al., 2012), it is on the low side of the temperature range of these previous reconstructions. A likely explanation for this difference is that the simulation of 'maximum' LGM extent corresponds to the earliest ice advances between 32.5±1.0 ka and 27.4±1.3 ka from the Lake Ōhau (Putnam et al., 2013a) or between 30 ka and 27 ka from the entire Southern Alps (Golledge et al., 2012), while we only constrain the latest stage of the LGM (19.8±0.3 ka) in this study. Our temperature depression also corresponds with pollen-based estimates of temperature lowering by 6.01±1.91°C for New Zealand at the ~21 ka (Newnham et al., 2013). Multiple studies showing excellent agreement give high confidence to these LGM temperature estimates, providing a robust target for assessment of paleoclimate simulations using climate models (e.g. Kageyama et al., 2017).

A close linkage between Southern Ocean sea surface temperatures (SSTs) and mid-latitude glacier activity was proposed by Barrows et al. (2007) and later supported by Doughty et al. (2015) and Shulmeister et al. (2018b). Sediment core MD97-2120, 300 km east from the Southern Alps at 45°S (Pahnke et al., 2003) and sediment core MD88-770 (R/V Marion Dufresne), situated southwest of Australia at 46°S (Barrows et al., 2007) (Figure 1) highlight a Southern Ocean temperature drops of 4-5°C below present at the height of the Last Glacial Maximum (Figure 9). Overall, the agreement between the estimated age of the Ahuriri moraine belt-3 and the cooling at ~20 ka years ago suggests that the deposition of this moraine was not a local event. Rather, it was likely caused by regional or hemispheric cooling during at this time.

5.2 Last glacial termination

5.2.1 Onset of glacier retreat

The former Ahuriri Glacier retreated from the prominent LGM terminal moraine (moraine belt-3) at or shortly after 19.8±0.3 ka. A flight of left-lateral moraines situated 2-4 km upstream (44°21'6"S 169°39'24"E) from moraine belt-3 records the downwasting of the glacier at this time. We attempted to constrain the timing of this ice-thinning event by targeting the innermost moraine of the recessional sequence, termed here moraine belt-2 yield exposure ages from 9.9±0.3 ka to 12.2±0.5 ka. These dates are unusually young for their situation relative to LGM ice limits and morphostratigraphically inconsistent with the age of moraine belt-1 (16.7±0.3 ka), thus we do not believe these accurately reflect the timing of moraine-belt-2 deposition.

Anomalously young outliers are not uncommon in alpine moraine datasets (Heyman et al., 2011). However, young outliers are often isolated cases, that occur perhaps due to unrecognised surface erosion or rotation of individual boulders, and stand apart from a more secure population of samples that centre close to the true depositional age (e.g. sample AL-27-61 from moraine belt-3 in this study; Table 1). However, the clustering of inaccurate ages from moraine belt-2 ages suggests the cause is a process that worked more uniformly across these boulders. One possibility is that we have misinterpreted the genesis of this landform. Landslide and rock avalanches are frequent occurrences in the tectonically active Southern Alps, and can generate hummocky landforms of unconsolidated, poorly sorted sediment that resemble moraines (McColl and Davies, 2011). However, the position of this landform close to the centre of the valley away from nearby hillslopes, coupled with the relatively low-elevation valley sides that seem unlikely to generate large runout mass movements, leads us to rule out such a misinterpretation. Furthermore, the connection of our sample site (44°21'46"S, 169°38'15"E) to the clear flight of left-lateral moraines (44°21'6"S 169°39'24"E) that grade to moraine belt-3 gives us confidence that our samples were similarly deposited by the waning former glacier.

We consider that the consistent age underestimation of samples from moraine belt-2 is likely to represent suppression of ^{10}Be production due to submergence beneath a shallow water body that developed during glacier retreat. Earlier mapping by Tielidze et al. (2021) revealed multiple shorelines imprinted on the ice-contact slope of moraine belt-3, which indicate former lake existence with former water levels (~725, 734, and 740 m a.s.l., Figure 10a). Crucially, the elevation of the uppermost shoreline is higher than the elevation of the boulders sampled (727-738 m a.s.l., Table 1), indicating that the boulders could have been submerged by this former water body. Using a cosmogenic nuclide production model, which incorporates the recent muon production model of Balco (2017c; Method 1A), we show that in situ cosmogenic ^{10}Be production declines rapidly even in shallow water, largely due to the rapid attenuation of spallogenic production (Figure 10b).

As a further test, we undertook hypothetical modelling to explore the lake depths and duration of boulder submergence that could explain our observed ^{10}Be concentrations. We assume that the proglacial lake existed continuously for a single period (rather than drying and refilling repeatedly) and that this period of lake cover began at 19 ka, shortly after moraine belt-3 deposition. Figure 10c shows that if water depth above our samples was 1-5 m, then minor sub-aqueous production could occur, and such a shallow lake would need to persist for 7-15 kyr to produce our measure concentrations. However, water depths >5 m effectively shutoff production. Thus, for a deeper lake (>5 m), our concentrations would imply lake persistence for ~7 kyr. While the lake depth is poorly constrained, these insights suggest that our concentrations require persistence of a glacial lake in Ahuriri River valley at least until the onset of the Holocene Epoch (c. 12 ka). Progressively falling lake levels, as indicated by the mapped shorelines (Figure 9-10; Tielidze et al., 2021) may reflect down-cutting of the lake outlow into the glacio-fluvial outwash plains as indicated by the impressive flights of fluvial terraces situated immediately outboard of moraine belt-3 (Figure 5). Further chronological investigation of these sequences may afford critical examination of our inferred chronology of proglacial lake evolution.

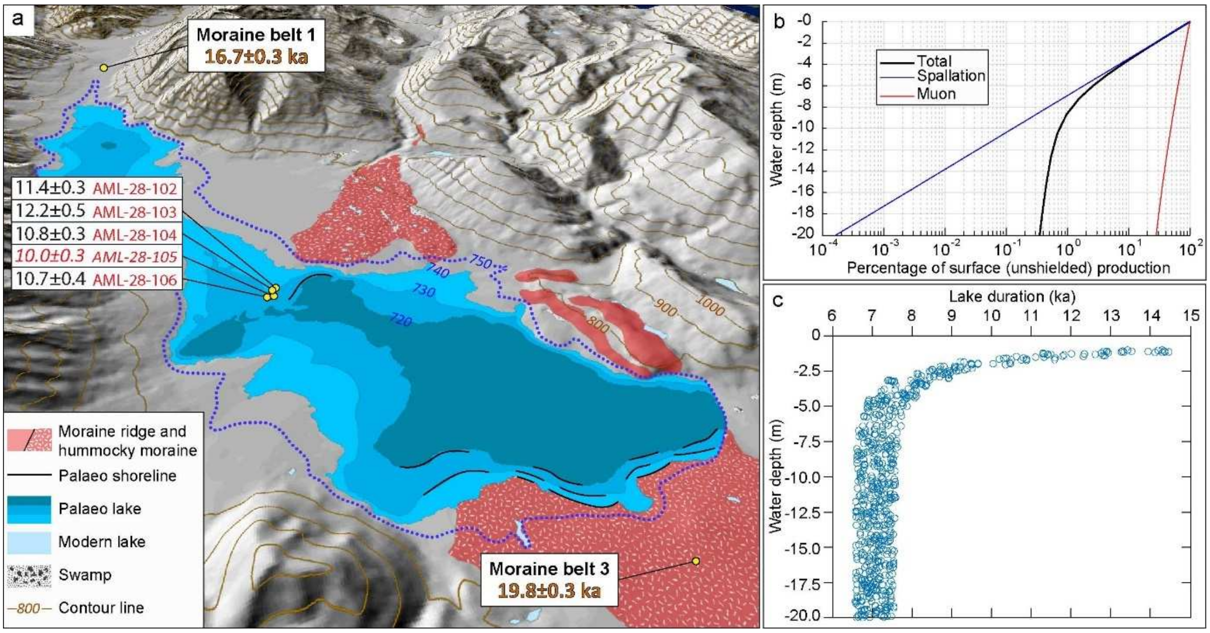

Figure 10. a – Five ^{10}Be exposure data from moraine belt-2 and simulated palaeo Lake Ahuriri. Lake bathymetry was provided according to the palaeo lake shorelines based on DEM contours. The blue dotted line shows the maximum possible level of the lake, where the hypothesised lake level coincides with the maximum elevation of the moraines. b – ^{10}Be production decreases beneath water according to Balco (2017c). c - hypothetical modelling to constrain the lake depths and duration of existence that could explain observed ^{10}Be concentrations.

5.2.2 Rate of deglacial warming

The available chronological information from the lower Ahuriri valley indicates that glacier retreat began at 19.8±0.3 ka, although the precise timing of ice withdrawal from the lower valley remains uncertain. However, surface-exposure ages from the moraine belt-1 confirm that the second re-advance or stillstand of the former Ahuriri Glacier occurred at 16.7±0.3 ka, which shows that a significant retreat of the palaeo Ahuriri Glacier occurred between 19.8±0.3 and 16.7±0.3 ka. These data constrain an 18 km retreat in glacier length (43% retreat of the LGM length) of the former Ahuriri Glacier. Our glacier reconstructions indicate that this retreat occurred in response to an ELA rise of c. 110 m, from ~1120 m a.s.l. to ~1230 m a.s.l., which corresponds to just 0.6°C of warming between those two time-periods (Figure 11) (assuming no change in precipitation occurred).

The large length change in response to relatively minor ELA rise suggests that the former Ahuriri glacier, in its LGM configuration, was highly sensitive to even minor climatic variability. Such high sensitivity may be a function of the very low inclination (~5 m/km) of the former Ahuriri Glacier in its middle to lower section (Figure 8). This characteristic of some former valley glaciers was recently demonstrated in the Cobb River valley, where physics-based modelling shows that a low-angle glacier reduced in length by half during the LGM in response to just 0.5°C rise in air temperature (Eaves et al., 2019). The former Ahuriri Glacier exhibits similar characteristics to former Cobb valley glacier, namely a low surface slope and lower altitude source area, especially in comparison to neighbouring Ōhau and Pukaki glaciers, which were sourced from the highest parts of the Southern Alps. These characteristics may be responsible for the observed difference in moraine sequences at these locations.

In contrast to the LGM, few quantitative estimates of air temperature changes during the last glacial termination exist for the Southern Alps. In one of the few glacial studies to provide such data, Putnam et al. (2013b) reported 3.25°C warming (from −6.25 to −3.0°C) between 17.8±0.2 and 16.3±0.4 ka from the Rakaia River valley, situated on the eastern side of the Southern Alps. At face value this rate of warming appears much greater than our ~0.6°C temperature increase between 19.8±0.3 ka and 16.7±0.3 ka (Figure 11), however there are several possible explanations for this discrepancy.

Firstly, it may represent a real difference, whereby there was substantial heterogeneity in the timing and rate of warming across the Southern Alps. The interplay of topography and atmospheric circulation, particularly the orientation of the Southern Alps relative to prevailing circulation, has been recognised to create distinct climate districts that exhibit different responses to changes in synoptic atmospheric conditions (Kidson, 2000; Lorrey et al., 2007; 2010). There is general consensus that the westerly winds contracted southwards during the last glacial termination (Anderson et al., 2009; Buizert et al., 2108; Denton et al., 2021), which would lead to an increase in blocking, relative to trough regimes (Kidson, 2000). However, such a regime shift tends to have fairly uniform temperature effects across the country, while flattening the west-east precipitation gradient (Lorrey et al., 2007). Neither of these climatic impacts are consistent with greater rates of recession of glaciers in the Rakaia, relative to the Ahuriri.

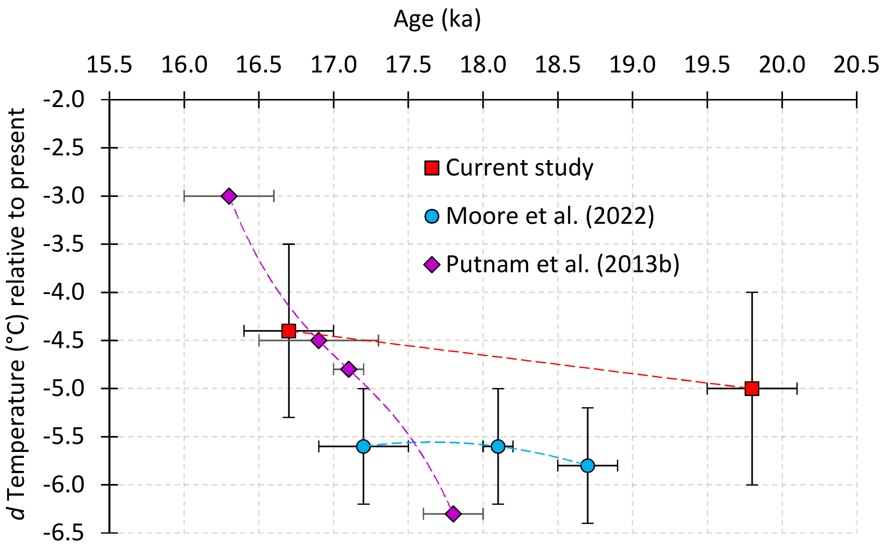

Figure 11. Comparison of the *d*Temperature (°C) change relative to present (1981-2010) between current study, Moore et al. (2022) and Putnam et al. (2013b) at the onset of last glacial termination.

Alternatively, both glacier-based temperature reconstructions may be accurate, but the difference may be caused by relatively low resolution of the dating method, relative to the rate of climate change. Despite precise local constraint of the in situ ^{10}Be production rate in New Zealand (Putnam et al., 2010), exposure ages of landforms typically have a 1σ (68% confidence interval) uncertainties of a few centuries at best, largely due to geological scatter. Thus, it is possible that this imprecision may reduce the ability to pinpoint the onset of deglaciation if those the climatic changes were abrupt (i.e. occurring over a few centuries or less) (Balco, 2020). This effect may be relevant to the onset of deglaciation in New Zealand. For example, Denton et al. (2021) demonstrate using climate model experiments how a southward shift in the westerly winds at the onset of the last glacial termination can cause several degrees of warming in the Tasman Sea over centennial timescales. Such a shift, which is supported by marine sea-surface temperature proxies (Bostock et al., 2015), may have occurred more rapidly than the cosmogenic dating method can resolve.

Recent studies have suggested that differences in the timing and rates of glacier retreat between nearby catchments may reflect local topo-climatic influence. For example, retreat of large valley glaciers, such as the former Rakaia Glacier, into overdeepened basins may have promoted proglacial lake formation that enhanced the overall sensitivity of glacier mass balance to atmospheric forcing

(Shulmeister et al., 2010). Sutherland et al. (2020) show that under similar climate conditions, glaciers calving into proglacial lakes may experience enhanced retreat relative to land-terminating glaciers. The modelling simulations of Putnam et al. (2013b) do not account for this possible feedback, likely due to the lack of constraint on former bed geometry, therefore it is possible their inferred temperature changes overestimate the rate of deglacial warming.

Finally, it is possible that methodological differences between our manual approach to ELA reconstructions and other numerical modelling approaches may be the cause of differences in the inferred temperature anomalies. Previous work has shown that temperature reconstructions are comparable between these methods (e.g. Kaplan et al., 2010; Doughty et al., 2013; Eaves et al., 2017), however these studies largely focus on relatively small former glaciers with simple geometries. Our application of manual glacier reconstruction method to the large, former Ahuriri Glacier requires extrapolation of ice surface over several 10s of kilometres without direct constraint by geomorphological evidence. Errors in the reconstructed glacier geometry may thus propagate over such distances with potential to impact the ELA estimation via the AAR method. However, temperature estimation via numerical modelling of former glaciers also involves assumptions (e.g. precipitation rate, bed geometry) that may cause inaccuracies (e.g. Rowan et al., 2014), which could also factor into the discrepancy between our deglacial temperature curve and that of Putnam et al. (2013b). It is noteworthy that a recent study from southern New Zealand demonstrates that the local ELA remained close to LGM values, with little evidence for warming, until at least 17.2±0.2 ka (Moore et al., 2022) (Figure 11). This reconstruction, from a simple former cirque glacier, is unlikely to be affected by uncertainties in past bed geometry or possible lake calving feedbacks, thus may represent a robust estimate of atmospheric conditions. Our record from the Ahuriri valley mirrors the ELA-inferred temperature changes from Moore et al. (2022), with gradual ELA-rises during the late stages of the LGM (see Eaves et al., 2019), with the majority of deglacial warming occurred after 17 ka.

5.2.3 Hypotheses for glacial termination and its triggering factors

A leading hypothesis for the last glacial termination suggests that Southern Hemisphere climate warming was triggered by rising Northern Hemisphere summer insolation intensity, which propagated southwards via oceanic and atmospheric teleconnections (Denton et al., 2010). Central to this hypothesis is the role of the oceanic bipolar seesaw mechanism, in which reduced North Atlantic Deep Water formation at 17.5 ka (McManus et al., 2004) caused sea surface warming across southern mid-high latitudes (Stocker and Johnsen, 2003; Pedro et al., 2018). However, while the timing of this proposed teleconnection correlates within dating uncertainties with the increases in glacier retreat rates in New Zealand (Putnam et al., 2013b), it does not readily explain the apparent early onset of gradual warming and glacier retreat recorded in the Ahuriri and other sites in the Southern Alps (Putnam et al., 2013a; Rother et al., 2014; Eaves et al., 2019; Moore et al., 2022).

Radiative equilibrium estimates by Huybers and Denton (2008) suggest an alternative insolation hypothesis – demonstrating that integrated summer duration over the Southern Ocean is near identical in timing and sign to northern (65°N) summer insolation intensity during the Late Pleistocene epoch. Denton et al. (2021) invoke this southern insolation hypothesis as a key driver of south-westerly winds position, which is important in explaining discrete shifts between glacial and interglacial modes of climate. The WAIS Divide team (2013) suggest such local insolation forcing may explain gradual warming over West Antarctica prior from 22-20 ka, as rising summer insolation reduced sea ice extent. According to Denton et al. (2021) such insolation changes may have also promoted gradual poleward shift of the southern westerly winds, permitting enhanced penetration of subtropical heat to southern mid-latitudes, which is consistent with our observations of retreating ice in the Southern Alps at this time. An advantage of this hypothesis is that it can reconcile these gradual changes with subsequent global deglaciation. Denton et al. (2021) demonstrate using a global climate model that a sustained poleward position of the westerlies from 18 ka (e.g. Buizert et al., 2018) can promote global-scale warming. Further model-based experiments are required to test this hypothesis further and disentangle competing influences such as rising carbon dioxide from 18 ka (e.g. Menviel et al., 2018).

6 Conclusions

To investigate the maximum extent and deglaciation of the former glacier during the Last Glacial Maximum, we report the first dataset from the Ahuriri River valley, central Southern Alps, New Zealand. The dataset includes 38 ^{10}Be surface-exposure ages from three different sites. The main findings of this study are:

i) The former Ahuriri Glacier reached its maximum extent at 19.8±0.3 ka. This advance appears to be the largest event of the last glacial cycle in the Ahuriri River valley.

ii) A GIS-based glacier reconstruction indicates that the palaeo Ahuriri Glacier had an ELA of 1170–1060 m a.s.l. at 19.8±0.3 ka, which is 830–940 m lower than the present ELA on nearby glaciers. This equates to a temperature difference of -5±1°C relative to present (1981-2010), which agrees within uncertainty with other regional climate proxy reconstructions for this time.

iii) Onset of glacier retreat after 19.8±0.3 ka coincided with development of a proglacial lake that imprinted shorelines on the LGM moraines and partially submerged recessional moraines. Anomalously young ^{10}Be exposure ages (11-12 ka) from submerged moraines suggest this lake persisted at c. 740 m a.s.l. or higher until at least 12 ka.

iv) By 16.7±0.3 ka the Ahuriri Glacier had retreated 18 km from its LGM position, in response to a c. 110 m rise in ELA, which equates to a 0.6°C rise in temperature. This small amount of warming contrasts with a previous estimate of local deglacial warming at this time interval from the Rakaia River valley (Putnam et al. 2013b). These differences may in part reflect the approaches taken to reconstruct past temperature from glaciers (ELA reconstructions using the AAR method versus glacier models), but the correspondence between this study and similar ELA-inferred temperature changes from Fiordland (Moore et al., 2022) shows that our finding may be real and warrants further investigation.

Our study shows that the Ahuriri Glacier was at its LGM position at 19.8±0.3 ka and then receded by 16.7±0.3 ka but our ages do not constrain the timing of termination onset. Thus, the precise timing of ice withdrawal from the lower Ahuriri valley remains uncertain. Further dating, particularly of the left lateral moraines near Moraine belt-2, may shed light on this.

Further work should focus on reconstructing paleo-ELAs from other regions through the deglaciation in New Zealand and comparing these with studies from similar mid latitude sites of former glaciation in South America and south-eastern Australia. This will help us build a more complete picture of the Late Quaternary glacial-climatic fluctuations in the Southern Hemisphere.

Credit author statement

Levan Tielidze: Conceptualization, Formal analysis, Investigation, Writing – original draft, Writing – review and editing, Visualization, Project administration. **Shaun Eaves**: Conceptualization, Formal analysis, Writing – original draft, Writing – review and editing, Visualization, Supervision, Funding acquisition, Project administration. **Kevin Norton**: Conceptualization, Writing – review and editing, Supervision, Funding acquisition, Project administration. **Andrew Mackintosh**: Conceptualization, Writing – review and editing, Supervision, Funding acquisition. **Alan Hidy**: Investigation, Writing – review and editing.

Declaration of competing interest

The authors declare that they have no known competing financial interests or personal relationships that could have appeared to influence the work reported in this paper.

Acknowledgements

We gratefully acknowledge the support of the editor, Colm O'Cofaigh, and two reviewers, James Shulmeister and Ann Rowan, for useful suggestions and detailed comments which clearly enhanced the quality of the paper. We are grateful to the landowners who permitted to work on their property. We thank Lisa Dowling and Emily Moore for help in the field.

Funding

This work was supported by Victoria University of Wellington and Marsden Fund - Royal Society of New Zealand (E3230). This work was performed in part under the auspices of the U.S. Department of

Energy by Lawrence Livermore National Laboratory under Contract DE-AC52- 07NA27344. This is LLNL-JRNL-820919.

References

Anderson, R. F., Ali, S., Bradtmiller, L. I., Nielsen, S. H. H., Fleisher, M. Q., Anderson, B. E., Burckle, L. H. (2009). Wind-driven upwelling in the Southern Ocean and the deglacial rise in atmospheric CO_2. Science 323, 1443-1448. DOI: 10.1126/science.1167441.

Balco, G., Stone, J. O., Lifton, N. A., Dunai, T. J. (2008). A complete and easily accessible means of calculating surface exposure ages or erosion rates from ^{10}Be and ^{26}Al measurements. Quat. Geochronol. 3, 174-195. doi.org/10.1016/j.quageo.2007.12.001.

Balco, G. (2011). Contributions and unrealized potential contributions of cosmogenic-nuclide exposure dating to glacier chronology, 1990-2010. Quaternary Science Reviews. 30 (1-2): p. 3-27. doi.org/10.1016/j.quascirev.2010.11.003.

Balco, G. (2017a). Documentation v3 exposure age calculator. Retrieved from https://sites.google.com/a/bgc.org/v3docs/home

Balco, G. (2017b). The online exposure age calculator formerly known as the CRONUS-Earth online exposure age calculator. Retrieved from https://hess.ess.washington.edu/math/v3/v3_age_in.html

Balco, G. (2017c). Production rate calculations for cosmic-ray-muon-produced ^{10}Be and ^{26}Al benchmarked against geological calibration data. Quaternary Geochronology. Vol. 39, pp. 150-173. https://doi.org/10.1016/j.quageo.2017.02.001.

Balco, G. (2020). Glacier Change and Paleoclimate Applications of Cosmogenic-Nuclide Exposure Dating. Annual Review of Earth and Planetary Sciences. 48:1, 21-48. doi.org/10.1146/annurev-earth-081619-052609.

Barr, I. D., and Lovell, H. (2014). A review of topographic controls on moraine distribution. Geomorphology, 226, 44-64. doi.org/10.1016/j.geomorph.2014.07.030.

Barrell, D. J.A., and Read, S. A.L. (2014). The deglaciation of Lake Pukaki, South Island, New Zealand - a review. New Zealand Journal of Geology and Geophysics, 57:1, 86-101. doi:10.1080/00288306.2013.847469.

Barrell, D. J. A. (2016). General distribution and characteristics of active faults and folds in the Waimate District and Waitaki District, South Canterbury and North Otago. GNS Science Consultancy Report 2015/166. 124 p.

Barrows, T. T., Stone, J. O., Fifield, L. K., and Cresswell, R. G. (2002). The timing of the Last Glacial Maximum in Australia, Quaternary Science Reviews, Vol. 21, 1–3, https://doi.org/10.1016/S0277-3791(01)00109-3.

Barrows, T. T., Juggins, S., De Deckker, P., Calvo, E., and Pelejero, C. (2007). Longterm sea surface temperature and climate change in the Australian-New Zealand region: Paleoceanography, v. 22, PA2215, doi:10.1029/2006PA001328.

Baumann, S. Anderson, B., Chinn, T., Mackintosh, A., Collier, C., Lorrey, A. M., Rack, W., Purdie, H., and Eaves, S. (2020). Updated inventory of glacier ice in New Zealand based on 2016 satellite imagery. Journal of Glaciology, 1–14. https://doi.org/10.1017/jog.2020.78.

Benn D. I. and Gemmell A. M. D. (1997). Calculating equilibrium-line altitudes of former glaciers by the balance ratio method: a new computer spreadsheet. Glacial Geol. Geomorphol. (1997), p. 7.

Borchers, B., Marrero, S., Balco, G., Caffee, M., Goehring, B., Lifton, N., Nishiizumi, K., Phillips, F., Schaefer, J., and Stone, J. (2016). Geological calibration of spallation production rates in the CRONUS-Earth project. Quaternary Geochronology, 31, 188-198. doi.org/10.1016/j.quageo.2015.01.009.

Bostock, H. C., Hayward, B. W., Neil, H. L., Sabaa, A. T., and Scott, G. H. (2015). Changes in the position of the Subtropical Front south of New Zealand since the last glacial period. Paleoceanography, 30, pp. 824-844. doi.org/10.1002/2014PA002652.

Buizert, C., Sigl, M., Severi, M. et al. (2018). Abrupt ice-age shifts in southern westerly winds and Antarctic climate forced from the north. Nature 563, 681–685. doi.org/10.1038/s41586-018-0727-5.

Carrivick J. L. and Chase S. E. (2011). Spatial and temporal variability of annual glacier equilibrium line altitudes in the Southern Alps, New Zealand, New Zealand Journal of Geology and Geophysics, 54:4, 415-429, DOI: 10.1080/00288306.2011.607463.

Chinn T., Fitzharris B. B., Willsman A., Salinger M. J. (2012). Annual ice volume changes 1976–2008 for the New Zealand Southern Alps. Global and Planetary Change 92: 105–118. doi.org/10.1016/j.gloplacha.2012.04.002.

Chinn, T. J, Kargel, J. S., Leonard, G. J., Haritashya, U. K. and Pleasants, M. (2014). New Zealand's Glaciers. In Global Land Ice Measurements from Space, Berlin, Heidelberg: Springer. pp. 675–715. doi: 10.1007/978-3-540-79818-7.

Clark, P. U., Dyke, A. S., Shakun, J. D. Carlson, A. E., Clark, J., Wohlfarth, B., Mitrovica, J. X., Hostetler, S. W. McCabe, A. M. (2009). The Last Glacial Maximum. Science. Vol. 325, Issue 5941, pp. 710-714. doi:10.1126/science.1172873.

Columbus, J., Sirguey, P., and Tenzer, R. (2011). A free, fully assessed 15-m DEM for New Zealand. Survey Quarterly, 66 , 16–19.

Darvill, C. M., Bentley, M. J., Stokes, C. R., and Shulmeister, J. (2016). The timing and cause of glacial advances in the southern mid-latitudes during the last glacial cycle based on a synthesis of exposure ages from Patagonia and New Zealand. Quaternary Science Reviews, 149, 200-214. Doi: doi.org/10.1016/j.quascirev.2016.07.024.

Denton, G. H., Anderson, R. F., Toggweiler, J. R., Edwards, R. L., Schaefer, J. M., and Putnam, A. E. (2010). The last glacial termination. Science, 328 (5986), pp. 1652-1656. doi: 10.1126/science.1184119.

Denton, G. H., Putnam, A. E., Russell, J. L., Barrell, D. J. A., Schaefer, J. M., Kaplan, M. R. and Strand, P. D. (2021). The Zealandia Switch: Ice age climate shifts viewed from Southern Hemisphere moraines, Quaternary Science Reviews, Vol. 257. 106771. doi.org/10.1016/j.quascirev.2020.106771.

Doughty, A. M., Anderson, B. M., Mackintosh, A. N., Kaplan, M. R., Vandergoes, M. J., Barrell, D. J. A., Denton, G. H., Schaefer, J. M., Chinn, T. J. H., and Putnam, A. E. (2013). Evaluation of Lateglacial temperatures in the Southern Alps of New Zealand based on glacier modelling at

Irishman Stream, Ben Ohau Range: Quaternary Science Reviews, Vol. 74, pp. 160-169. doi:10.1016/j.quascirev.2012.09.013.

Doughty, A. M., Schaefer, J. M., Putnam, A. E., Denton, G. H., Kaplan, M. R., Barrell, D. J. A., Andersen, B. G., Kelley, S. E., Finkel, R .C., Schwartz, R. (2015). Mismatch of glacier extent and summer insolation in Southern Hemisphere mid-latitudes. Geology, 43 (5): 407–410. doi:doi.org/10.1130/G36477.1.

Doughty, A. M., Mackintosh, A. N., Anderson, B. M., Dadic, R., Putnam, A. E., Barrell, D. J. A., Denton, G. H., Chinn, T. J. H. and Schaefer, J. M. (2017). An exercise in glacier length modeling: Interannual climatic variability alone cannot explain Holocene glacier fluctuations in New Zealand. Earth and Planetary Science Letters. Vol. 470, pp. 48-53. doi.org/10.1016/j.epsl.2017.04.032.

Dowling, L. Eaves, S. Norton, K. Mackintosh, A. Anderson, B. Hidy, A. Lorrey, A. Vargo, L. Ryan, M., and Tims, S. (2021). Local summer insolation and greenhouse gas forcing drove warming and glacier retreat in New Zealand during the Holocene. Quaternary Science Reviews, Vol. 266, p. 107068. doi.org/10.1016/j.quascirev.2021.107068.

Eaves, S. R., Mackintosh, A. N., Anderson, B. M., Doughty, A. M., Townsend, D. B., Conway, C. E., Winckler, G., Schaefer, J. M., Leonard, G. S., and Calvert, A. T. (2016). The Last Glacial Maximum in the central North Island, New Zealand: Paleoclimate inferences from glacier modelling: Climate of the Past, v. 12, p. 943–960, https:// doi .org /10 .5194 /cp -12 -943 -2016.

Eaves, S. R., Anderson, B. M., and Mackintosh, A. N. (2017). Glacier-based climate reconstructions for the last glacial–interglacial transition: Arthur’s Pass, New Zealand (42° S): Journal of Quaternary Science, v. 32, p. 877–887, https:// doi .org /10 .1002 /jqs .2904.

Eaves, S. R., Mackintosh, A. N., and Anderson, B. M. (2019). Climate amelioration during the Last Glacial Maximum recorded by a sensitive mountain glacier in New Zealand. Geology (2019) 47 (4): 299–302. https://doi.org/10.1130/G45543.1.

García, J., Maldonado, A., De Porras, M., Nuevo Delaunay, A., Reyes, O., Ebensperger, C., Binnie, S., Lüthgens, C. and Méndez, C. (2019). Early deglaciation and paleolake history of Río Cisnes

Glacier, Patagonian Ice Sheet (44°S). Quaternary Research, 91(1), 194-217. doi:10.1017/qua.2018.93.

Gibbons, A. B., Megeath, J. D. and Pierce, K. L. (1984). Probability of moraine survival in a succession of glacial advances. Geology, 12(6), pp. 327-330. doi.org/10.1130/0091-7613(1984)12<327:POMSIA>2.0.CO;2.

Golledge, N. R., Mackintosh, A. N., Anderson, B. M., Buckley, K. M., Doughty, A. M., Barrell, D. J. A., Denton, G. H., Vandergoes, M. J., Andersen, B. G. and Schaefer, J. M. (2012). Last Glacial Maximum climate in New Zealand inferred from a modelled Southern Alps icefield, Quaternary Science Reviews, Vol. 46, pp. 30-45, doi.org/10.1016/j.quascirev.2012.05.004.

Granshaw F. D. and Fountain A. G. (2006). Glacier change (1958–1998) in the North Cascades National Park Complex, Washington, USA, J. Glaciol., 52, 251–256, doi.org/10.3189/172756506781828782.

Heyman, J. Stroeven, A. P., Harbor, J. M., and Caffee, M. W. (2011). Too young or too old: evaluating cosmogenic exposure dating based on an analysis of compiled boulder exposure ages. Earth and Planetary Science Letters 302, 71–80. https://doi.org/10.1016/j.epsl.2010.11.040.

Huybers, P. and Denton, G. (2008). Antarctic temperature at orbital timescales controlled by local summer duration. Nature Geosci 1, 787–792. doi.org/10.1038/ngeo311.

IPCC (2019). Special report on the ocean and cryosphere in a changing climate. Geneva, Switzerland 1 (3).

Kageyama, M., Albani, S., Braconnot, P., Harrison, S. P., Hopcroft, P. O., Ivanovic, R. F., Lambert, F., Marti, O., Peltier, W. R., Peterschmitt, J. Y. and Roche, D. M. (2017). The PMIP4 contribution to CMIP6–Part 4: Scientific objectives and experimental design of the PMIP4-CMIP6 Last Glacial Maximum experiments and PMIP4 sensitivity experiments. Geoscientific Model Development, 10(11), pp.4035-4055. https://doi.org/10.5194/gmd-10-4035-2017, 2017.

Kalm, V., Mahaney, M. C. (2011). Late Quaternary glaciations in the Venezuelan (Mérida) Andes. In: Ehlers, J., Gibbard, P. L., Hughes, P.D. (Eds.), Quaternary Glaciations — Extent and Chronology: A Closer Look. Developments in Quaternary Science, 16. Elsevier, Amsterdam, pp. 835–842. doi.org/10.1016/B978-0-444-53447-7.00059-3.

Kamp, P. and Tippett, J. (1993). Dynamics of the Pacific Plate crust in the South Island (New Zealand) zone of oblique continent-continent convergence. Journal of Geophysical Research, 98: 105–116.

Kaplan, M. R., Fogwill, C. J., Sugden, D. E., Hulton, N. R. J., Kubik, P. W., Freeman, S. P. H. T. (2008). Southern Patagonian glacial chronology for the Last Glacial period and im-plications for Southern Ocean climate. Quat. Sci. Rev. 27, 284–294. doi.org/10.1016/j.quascirev.2007.09.013.

Kaplan, M. R., Schaefer, J. M., Denton, G. H., Barrell, D. J. A., Chinn, T. J. H., Putnam, A. E., Andersen, B. G., Finkel, R. C., Schwartz, R., Doughty, A. M. (2010). Glacier retreat in New Zealand during the Younger Dryas Stadial. Nature 467, 194-197. doi.org/10.1038/nature09313.

Kidson, J. W. (2000). An analysis of New Zealand synoptic types and their use in defining weather regimes. International Journal of Climatology 20: 299–316. doi.org/10.1002/(SICI)1097-0088(20000315)20:3<299::AID-JOC474>3.0.CO;2-B.

Kiernan, K., Fifield, L., and Chappell, J. (2004). Cosmogenic nuclide ages for Last Glacial Maximum moraine at Schnells Ridge, Southwest Tasmania. Quaternary Research, 61(3), 335-338. doi:10.1016/j.yqres.2004.02.004.

Kirkbride, M. P., Brazier V. (1998). A critical evaluation of the use of glacier chronologies in climatic reconstruction, with reference to New Zealand. In L.A. Owen (Ed.), Mountain Glaciation, Quaternary Proceedings N6, Wiley, Chichester, pp. 55-64.

Kohl, C.P. and Nishiizumi, K. (1992). Chemical isolation of quartz for measurement of in-situ - produced cosmogenic nuclides. Geochimica et Cosmochimica Acta. Vol. 56, 9, pp. 3583-3587. https://doi.org/10.1016/0016-7037(92)90401-4.

Lamont, G. N., Chinn, T. J., and Fitzharris, B. B. (1999). Slopes of glacier ELAs in the Southern Alps of New Zealand in relation to atmospheric circulation patterns. Glob. Planet. Change 22, 209–219. doi: 10.1016/S0921-8181(99)00038-7.

Leger, T. P. M., Hein, A. S., Bingham, R. G., Rodés, Á., Fabel, D., and Smedley, R. K. (2021). Geomorphology and 10Be chronology of the Last Glacial Maximum and deglaciation in northeastern Patagonia, 43°S-71°W, Quaternary Science Reviews, Vol. 272, 107194, doi.org/10.1016/j.quascirev.2021.107194.

Lifton, N., Sato, T. and Dunai, T. J. (2014). Scaling in situ cosmogenic nuclide production rates using analytical approximations to atmospheric cosmic-ray fluxes. Earth and Planetary Science Letters, 386, 149-160. doi.org/10.1016/j.epsl.2013.10.052.

Lorrey, A., Fowler A. M., and Salinger, J. (2007). Regional climate regime classification as a qualitative tool for interpreting multi-proxy palaeoclimate data spatial patterns: A New Zealand case study. Palaeogeography, Palaeoclimatology, Palaeoecology. 253. pp. 407-433. doi:10.1016/j.palaeo.2007.06.011.

Lorrey, A. M, Vandergoes, M., Renwick. J, et al. (2010). A regional climate regime classification synthesis for New Zealand covering three critical periods of the late Quaternary: The last 2000 years, the mid-Holocene, and the end of the Last Glacial Coldest Period. NIWA Client Report AKL2010-025 prepared for the University of Auckland.

Lorrey, A. M., and Bostock, H. (2017). The Climate of New Zealand Through the Quaternary. In: Shulmeister J. (eds) Landscape and Quaternary Environmental Change in New Zealand. Atlantis Advances in Quaternary Science, vol 3. Atlantis Press, Paris. doi.org/10.2991/978-94-6239-237-3_3.

Lukas S. (2007). Early-Holocene glacier fluctuations in Krundalen, south central Norway: palaeo-glacier dynamics and palaeoclimate. Holocene, 17, pp. 585-598. doi.org/10.1177/0959683607078983.

Mackintosh, A. N., Barrows, T. T., Colhoun, E. A., and Fifield, L. K. (2006). Exposure dating and glacial reconstruction at Mt. Field, Tasmania, Australia, identifies MIS 3 and MIS 2 glacial advances and climatic variability. J. Quaternary Sci., Vol. 21 pp. 363–376. https://doi.org/10.1002/jqs.989.

Mackintosh, A. N., Anderson, B. M., and Pierrehumbert, R. T. (2017). Reconstructing climate from glaciers. Annu. Rev. Earth Planet. Sci. 45:649–80. doi.org/10.1146/annurev-earth-063016-020643.

McColl, S. T., and Davies, T. R. (2011). Evidence for a rock-avalanche origin for 'The Hillocks'"moraine", Otago, New Zealand. Geomorphology, 127(3-4), pp.216-224. doi.org/10.1016/j.geomorph.2010.12.017.

McKinnon, K. A., Mackintosh, A. N., Anderson, B. M., Barrell, D. J. A. (2012). The influence of sub-glacial bed evolution on ice extent: a model-based evaluation of the Last Glacial Maximum Pukaki glacier, New Zealand. Quat. Sci. Rev. 57, 46-57. doi.org/10.1016/j.quascirev.2012.10.002.

McManus, J. F., Francois, R., Gherardi, J. M., Keigwin, L. D. and Brown-Leger, S. (2004). Collapse and rapid resumption of Atlantic meridional circulation linked to deglacial climate changes. nature, 428(6985), pp.834-837. doi.org/10.1038/nature02494.

Menviel, L., Spence, P., Yu, J., Chamberlain, M.A., Matear, R.J., Meissner, K.J. and England, M.H. (2018). Southern Hemisphere westerlies as a driver of the early deglacial atmospheric CO 2 rise. Nature Communications, 9(1), pp.1-12. doi.org/10.1038/s41467-018-04876-4.

Meier, M. F., Post, A. S., 1962. Recent Variations in Mass Net Budgets of Glaciers in Western North America. International Association of Scientific Hydrology Publication, pp. 63-77, 58.

Moore, E. M. M., Eaves, S. R., Norton, K. P., Mackintosh, A. N. Anderson, B. M., Dowling, L. H., Hidy, A. J. (2022). Climate reconstructions for the Last Glacial Maximum from a simple cirque glacier in Fiordland, New Zealand. Quaternary Science Reviews 275, 107281. doi.org/10.1016/j.quascirev.2021.107281.

Newnham, R., McGlone, M., Moar, N., Wilmshurst, J. and Vandergoes, M. (2013). The vegetation cover of New Zealand at the Last Glacial Maximum: Quaternary Science Reviews, v. 74, p. 202–214, doi.org /10 .1016 /j .quascirev .2012 .08 .022.

Nesje A. and Dahl S. O. (2000). Glaciers and Environmental Change. New York: Oxford University Press. 216 pp. ISBN 9780340706343.

Nishiizumi K., Imamura M., Caffee M. W., Southon J. R., Finkel R. C. and McAninch J. (2007). Absolute calibration of 10Be AMS standards. Nucl. Instrum. Methods Phys. Res. Sect. B Beam Interact. Mater. Atoms. 258, 403-413. doi.org/10.1016/j.nimb.2007.01.297.

NIWA (National Institute of Water and Atmospheric Research). (2012). New Zealand median annual average temperature based on 30 year period 1981-2010.

Norris, R. J., and Cooper, A. F. (2001). Late quaternary slip rates and their significance for slip partitioning on the Alpine Fault. Journal of Structural Geology, 23(2/3): 507-520.

Norton, D. (1985). A multivariate technique for estimating New Zealand temperature normals. Weather and Climate 5, 64-74. doi:10.2307/44279988.

Ochs, M. and Ivy-Ochs, S. (1997). The chemical behavior of Be, Al, Fe, Ca and Mg during AMS target preparation from terrestrial silicates modeled with chemical speciation calculations. Nuclear Instruments and Methods in Physics Research Section B: Beam Interactions with Materials and Atoms. Vol. 123, 1–4, pp. 235-240. https://doi.org/10.1016/S0168-583X(96)00680-5.

Oerlemans, J. and Fortuin, J. P. F. (1992). Sensitivity of glaciers and small ice caps to greenhouse warming, Science, 258, 115–117, doi:10.1126/science.258.5079.115.

Oerlemans, J. (2005). Extracting a Climate Signal from 169 Glacier Records. Science. Vol. 308, Issue 5722, pp. 675-677. doi:10.1126/science.1107046.

Ohmura, A., Kasser, P. and Funk, M. (1992). Climate at the equilibrium line of glaciers. Journal of Glaciology 38, 397–411. https://doi.org/10.3189/S0022143000002276.

Pahnke, K., Zahn, R., Elderfield, H., and Schulz, M. (2003). 340,000-year centennial- scale marine record of Southern Hemisphere climatic oscillation: Science, v. 301, p. 948–952, doi:10.1126/science.1084451.

Pellitero R., Rea B. R., Spagnolo M., Bakke J., Hughes P., Ivy-Ochs S., Lukas S., and Ribolini A. (2015). A GIS tool for automatic calculation of glacier equilibrium-line altitudes, Computers and Geosciences. Vol. 82, pp. 55-62. doi.org/10.1016/j.cageo.2015.05.005.

Pedro, J. B., Rasmussen, S. O. and van Ommen, T. D. (2012). Tightened constraints on the time-lag between Antarctic temperature and CO_2 during the last deglaciation, Clim. Past, 8, 1213–1221, doi.org/10.5194/cp-8-1213-2012.

Pedro, J. B., Jochum, M., Buizert, C., He, F., Barker, S. and Rasmussen, S. O. (2018). Beyond the bipolar seesaw: Toward a process understanding of interhemispheric coupling. Quaternary Science Reviews 192, 27-46. doi.org/10.1016/j.quascirev.2018.05.005.

Porter, S. C. (1975). Equilibrium-line altitudes of late Quaternary glaciers in the Southern Alps, New Zealand. Quaternary Research 5, 27-47. doi.org/10.1016/0033-5894(75)90047-2.

Porter, S. (2001). Snowline depression in the tropics during the Last Glaciation. Quaternary Science Reviews. Vol. 20, pp. 1067-1091. doi.org/10.1016/S0277-3791(00)00178-5.

Putnam, A. E., Schaefer, J. M., Barrell, D. J. A., Vandergoes, M., Denton, G. H., Kaplan, M. R., Schwartz, R., Finkel, R. C., Goehring, B. M., Kelley, S. E. (2010). In situ cosmogenic ^{10}Be production rate calibration from the Southern Alps, New Zealand. Quaternary Geochronology. 5, 392–409. doi.org/10.1016/j.quageo.2009.12.001.

Putnam A. E., Schaefer, J. M., Denton G. H. et al. (2012). Regional climate control of glaciers in New Zealand and Europe during the preindustrial Holocene. Nature Geoscience 5: 627-630. doi.org/10.1038/ngeo1548.

Putnam, A. E., Schaefer, J. M., Denton, G. H., Barrell, D. J. A., Birkel, S. A., Andersen, B. G., Kaplan, M. R., Finkel, R. C., Schwartz, R., Doughty, A. M. (2013a). The Last Glacial Maximumat 44°S documented by a moraine chronology at Lake Ohau, Southern Alps of New Zealand. Quaternary Science Reviews 62, 114–141. doi.org/10.1016/j.quascirev.2012.10.034.

Putnam, A. E., Schaefer, J. M., Denton, G. H., et al. (2013b). Warming and glacier recession in the Rakaia valley, Southern Alps of New Zealand, during Heinrich Stadial 1. Earth and Planetary Science Letters 382: 98–110. doi.org/10.1016/j.epsl.2013.09.005.

Purdie, H., Anderson, B., Chinn, T., Owen, I., Mackintosh, A. and Lawson, W. (2014). Franz Josef and Fox Glaciers, New Zealand: Historic length records. Global and Planetary Change. Vol. 121, pp. 41-52. doi.org/10.1016/j.gloplacha.2014.06.008.

Rattenbury, M. S.; Jongens, R.; Cox, S. C. (compilers) 2010: Geology of the Haast area: scale 1:250,000. Lower Hutt: Institute of Geological & Nuclear Sciences Limited. Institute of Geological & Nuclear Sciences 1:250,000 geological map 14. 67 p. + 1 folded map.

Rother, H., Fink, D., Shulmeister, J., Mifsud, C., M. Evans and Pugh, J. (2014). The early rise and late demise of New Zealand's last glacial maximum. Proceedings of the National Academy of Science, 111, 11630-11635. https://doi.org/10.1073/pnas.1401547111.

Rowan, A. V., Brocklehurst, S. H., Schultz, D. M., Plummer, M. A., Anderson, L. S., and Glasser, N. F. (2014). Late Quaternary glacier sensitivity to temperature and precipitation distribution in the Southern Alps of New Zealand, Journal of Geophysical Research: Earth Surface, 119, 1064– 1081, doi:10.1002/2013JF003009.

Stone, J. (2000). Air pressure and cosmogenic isotope production. Journal of Geophysical Research. Solid Earth, Vol. 105. NO. B10, 23,753-23,759. doi.org/10.1029/2000JB900181.

Strand, P. D. Schaefer, J. M., Putnam, A. E., Denton, G. H., Barrell, D. J. A., Koffman, T. N. B. and Schwartz, R. (2019). Millennial-scale pulsebeat of glaciation in the Southern Alps of New Zealand. Vol. 220, pp.165-177. doi.org/10.1016/j.quascirev.2019.07.022.

Strelin, J. A., Denton, G. H., Vandergoes, M. J., Ninnemann, U. S. and Putnam A. E. (2011). Radiocarbon chronology of the late-glacial Puerto Bandera moraines, Southern Patagonian Icefield, Argentina. Quat. Sci. Rev., 30 (2011), pp. 2551-2569. doi.org/10.1016/j.quascirev.2011.05.004.

Shulmeister, J., Fink, D., Hyatt, O. M., Thackray, G. D., and Rother, H. (2010). Cosmogenic ^{10}Be and ^{26}Al exposure ages of moraines in the Rakaia Valley, New Zealand and the nature of the last termination in New Zealand glacial systems. Earth and Planetary Science Letters. Vol. 297, Issues 3–4, pp. 558-566. doi.org/10.1016/j.epsl.2010.07.007.

Shulmeister, J., Fink, D., Winkler, S., Thackray, G. D., Borsellino, R., Hemmingsen, M., and Rittenour, T. M. (2018a). Evidence for slow late-glacial ice retreat in the upper Rangitata Valley, South Island, New Zealand. Quaternary Science Reviews, Vol. 185, pp. 102-112. doi.org/10.1016/j.quascirev.2018.01.006.

Shulmeister, J., Thackray, G. D., Rittenour, T., and Hyatt, O. M. (2018b). Multiple glacial advances in the Rangitata Valley, South Island, New Zealand, during the last glaciation imply substantial extent and duration of MIS 3 glaciation. Quaternary Research. 89, 375-393 doi:10.1017/qua.2017.108.

Sime, L. C., Kohfeld, K. E., Le Quéré, C., Wolff, E. W., de Boer, A. M., Graham, R. M., & Bopp, L. (2013). Southern Hemisphere westerly wind changes during the Last Glacial Maximum: model-data comparison. Quaternary Science Reviews, 64, 104-120. Doi: doi.org/10.1016/j.quascirev.2012.12.008.

Stocker, T. F. and Johnsen, S. J. (2003). A minimum thermodynamic model for the bipolar seesaw, Paleoceanography, 18, 1087, doi:10.1029/2003PA000920, 4.

Sutherland, J. L., Carrivick, J. L., Gandy, N., Shulmeister, J., Quincey, D. J., and Cornford, S. L. (2020). Proglacial lakes control glacier geometry and behavior during recession. Geophysical Research Letters, 47, e2020GL088865. doi.org/10.1029/2020GL088865.

Tait, A. and Macara, G. (2014). Evaluation of interpolated daily temperature data for high elevation areas in New Zealand. Weather and Climate, Vol. 34. pp. 36-49.

Tielidze, L. G. and Wheate, R. D. (2018). The Greater Caucasus Glacier Inventory (Russia, Georgia and Azerbaijan), The Cryosphere, 12, 81–94, doi.org/10.5194/tc-12-81-2018.

Tielidze L. G., Eaves S. R., Norton, K. P., and Mackintosh A. N. (2021). Glacial geomorphology of the Ahuriri River valley, central Southern Alps, New Zealand, Journal of Maps, 17:2, 73-86, doi: 10.1080/17445647.2021.1876777.

Turnbull, I. M. (compiler) 2000: Geology of the Wakatipu area: scale 1:250,000. Lower Hutt: Institute of Geological & Nuclear Sciences. Institute of Geological & Nuclear Sciences 1:250,000 geological map 18. 72 p. + 1 folded map.

WAIS Divide Project Members. (2013). Onset of deglacial warming in West Antarctica driven by local orbital forcing. Nature 500, 440–444. doi.org/10.1038/nature12376.

Williams, P. W. (1991). Tectonic geomorphology, uplift rates and geomorphic response in New Zealand. CATENA. Vol. 18, Issue 5, pp. 439-452. doi.org/10.1016/0341-8162(91)90048-3.